Research Square

Preprints are preliminary reports that have not undergone peer review.
They should not be considered conclusive, used to inform clinical practice,
or referenced by the media as validated information.

Geometry-dependent sediment pressure in salt caverns: A Janssen-based formulation validated against coupled simulations

Hao Zhang
China University of Mining and Technology
Guimin Zhang
gmzhang@cumt.edu.cn

China University of Mining and Technology
Yuxuan Liu
Chery Automobile (China)
Yibo Wu
China University of Mining and Technology
Peng Li
Chinese Academy of Sciences
Xilin Shi
Chinese Academy of Sciences
Yinping Li
Chinese Academy of Sciences

Research Article

Keywords: Salt cavern energy storage, sediment pressure, PFC3D-FLAC3D coupling, Janssen's theory, stability analysis

Posted Date: November 17th, 2026

DOI: https://doi.org/10.21203/rs.3.rs-11456581/v1

License: This work is licensed under a Creative Commons Attribution 4.0 International License.
Read Full License

Additional Declarations: No competing interests reported.

Geometry-dependent sediment pressure in salt caverns: A Janssen-based formulation validated against coupled simulations

Hao Zhang[a], Guimin Zhang[a,c*], Yuxuan Liu[b**], Yibo Wu[a], Peng Li[d], XiLin Shi[d], YinPing Li[d]

[a] *State Key Laboratory of Intelligent Construction and Healthy Operation and Maintenance of Deep Underground Engineering, School of Mechanics and Civil Engineering, China University of Mining and Technology, Xuzhou, Jiangsu, 221116, China;*

[b] *Chery Automobile Co., Ltd., Wuhu, Anhui 241007, China;*

[c] *School of Energy, China University of Mining and Technology, Xuzhou, Jiangsu, 221116, China;*

[d] *State Key Laboratory of Geomechanics and Geotechnical Engineering, Institute of Rock and Soil Mechanics, Chinese Academy of Sciences, Wuhan, Hubei, 430071, China;*

** E-mail address of corresponding author (**Guimin Zhang**):* **gmzhang@cumt.edu.cn**

*** E-mail address of corresponding author (**Yuxuan Liu**):* **liuyuxuan11@mychery.com**

Abstract: A large amount of sediment is generated during salt cavern construction by solution mining in China's bedded salt rock. The highly connected pore structure inside the sediment has considerable energy storage potential, which urgently requires further development. However, as a key factor affecting the stability of salt cavern gas storage, the method for calculating sediment pressure remains to be improved. Based on the Janssen equation, this study established a calculation method for the normal pressure exerted by sediment on the salt cavern wall under the condition of continuous solution mining in high-impurity salt mines. This method was embedded into FLAC^{3D} as a validation model, and comparative verification was conducted with a benchmark model constructed using PFC^{3D}-FLAC^{3D} coupled numerical simulation. The results show that: (1) This method can significantly improve computational efficiency with small errors: the sediment pressure error is less than 0.03 MPa, the absolute error of cavern wall displacement is less than 5 mm, and the relative error of cavern wall displacement is less than 5%; (2) The sediment pressure distribution is significantly influenced by cavern geometry and sediment accumulation height, whereas the effect of cavern radius is relatively limited. When the friction coefficient between the sediments and cavern wall is relatively large, the normal pressure may decrease locally near the cavern bottom; (3) Under low operating gas pressure conditions, the enhancement effect of sediment on salt cavern stability has non-negligible engineering value.

Keywords: Salt cavern energy storage; sediment pressure; PFC^{3D}-FLAC^{3D} coupling; Janssen's theory; stability analysis

1. Introduction

Salt deposits occur at depths ranging from several hundred meters to as much as 4000 m below the ground surface (Liu et al. 2023; Li et al. 2024). Caverns formed through solution mining provide suitable storage sites for compressed air, hydrogen, helium (Wei et al. 2024), and other resources. Feasibility studies on salt cavern energy storage are currently being conducted in many countries (Kumar et al. 2021; Martin-Clave et al. 2021; Cyran 2021; Fatah et al. 2024; Wang et al. 2024a). Most salt deposits in China are of lacustrine origin and are characterized by distinct depositional cyclicity and numerous interlayers between salt beds (Zhang et al. 2015, 2021a; Li et al. 2018; Liu et al. 2020). During solution mining, insoluble materials in bedded rock salt settle at the cavern bottom and form sediments (Gao et al. 2005; Ge et al. 2023; Ren et al. 2017). Previous studies have shown that accumulated sediments reduce gas storage efficiency and may cause well tubing blockage (Liu, 2011; Wang et al. 2021; Vitali and Vitali 2024; Ye et al. 2025). However, other studies (Li et al. 2022, 2023) have also indicated that sediments can enhance salt cavern stability to some extent (Qu et al. 2012; Wang et al. 2023).

In the early 2000s, pilot gas storage facilities were constructed in Jintan, Jiangsu Province, where geological conditions are relatively favourable. Engineers and researchers primarily investigated the effects of operating pressure, cavern geometry, and pillar width on the stability of the surrounding rock (Khaledi et al. 2016; Djizanne et al. 2014; Yan et al. 2022; Zhang et al. 2017a; Cording et al. 2015). However, the influence of sediments on cavern

stability was not considered in these early studies (Wang et al. 2013, 2015; Ma et al. 2015; Zhang et al. 2017b; Ma et al. 2013; Deng et al. 2014). This was mainly because the Jintan Basin contains thick, high-grade salt beds, and the sediments accumulated at the cavern bottom after cavern construction accounted for only approximately 25% of the total cavern volume (Li et al. 2016a). Overall, the influence of sediments on salt cavern stability in the Jintan area was relatively limited.

Following the successful operation of the Jintan gas storage facilities, pilot gas storage projects were initiated in several other regions, including Yingcheng in Hubei Province, Huai'an in Jiangsu Province, and Feicheng in Shandong Province. Unlike Jintan, salt formations in these regions commonly exhibit one or both of the following characteristics: thick interlayers and low-grade rock salt (high impurity content). These geological conditions result in the generation of large amounts of sediments during cavern construction, with sediment volumes sometimes exceeding 60% of the total cavern volume (Wei et al. 2023; Zhang et al. 2017c, 2024). Given the generally loose packing and high internal connectivity of the sediments, numerous researchers have proposed utilizing the pore space within the sediments for gas storage (Li et al. 2016b; Sun et al. 2024; Liang et al. 2023a, 2023b; Wang et al. 2020). However, under the action of gravity, accumulated sediments exert varying degrees of pressure on the cavern walls. Considering the substantial increase in sediment volume and the critical role of sediments in the proposed utilization of sediment pore space for gas storage, their influence on cavern stability assessments can no longer be neglected. Therefore, a reliable method for calculating the pressure exerted by sediments on cavern walls in high-impurity salt deposits is urgently needed.

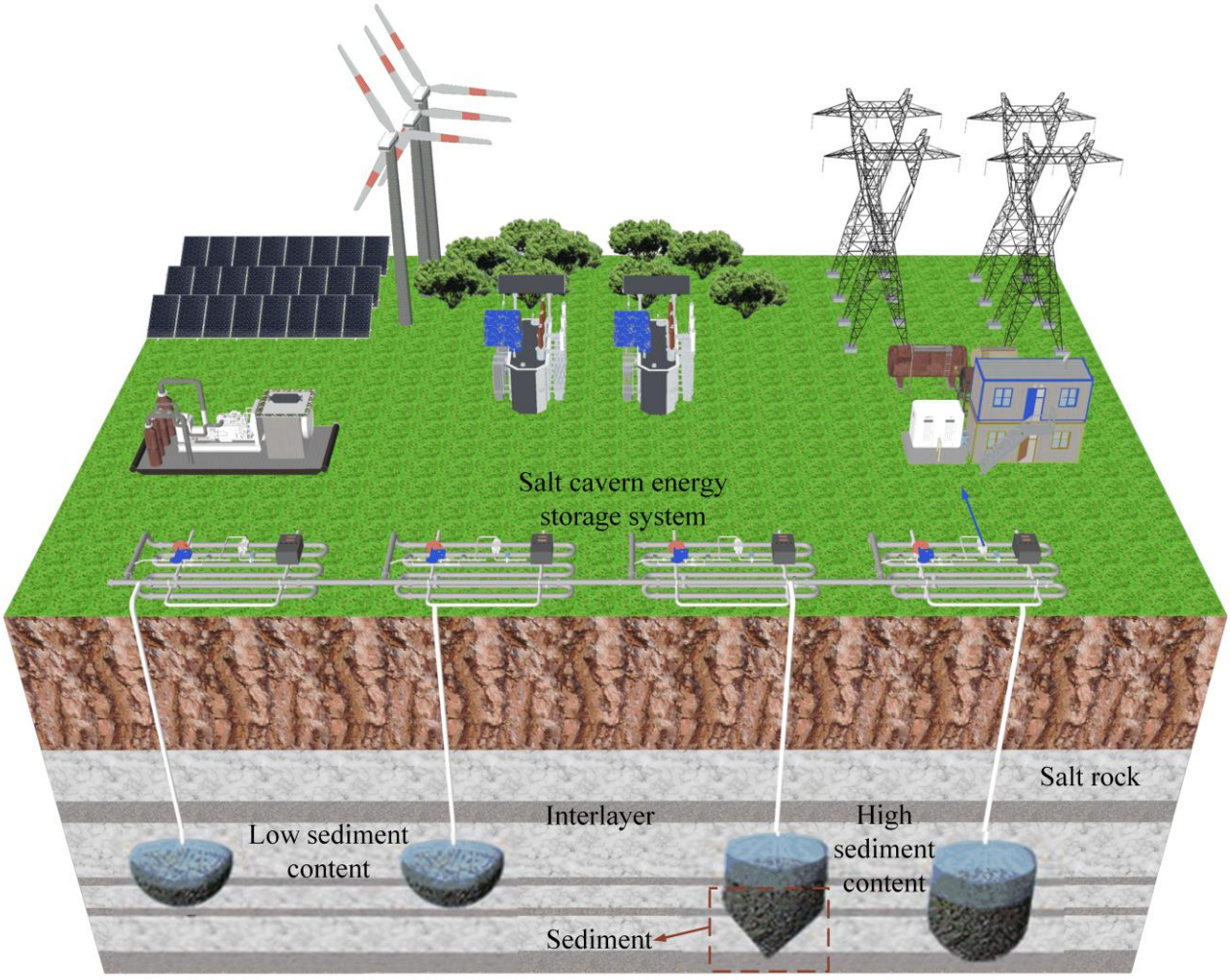


Fig. 1. Salt cavern energy storage power plant

In numerical simulations conducted to assess the stability of salt cavern gas storage facilities, the forces exerted by sediments are generally represented as normal pressures to facilitate their application to cavern wall surfaces. Currently, commonly used calculation methods treat sediments as an undisturbed rock mass, assuming an ideal linear relationship between pressure and depth (Fu et al. 2025). However, sediments are composed of discrete, packed materials and differ substantially from the continuous intact rock mass. Consequently, the application of these methods may introduce considerable errors, thereby affecting the accuracy of salt cavern stability assessments. Therefore, further investigation into methods for calculating the normal pressure exerted by sediments is necessary.

The Janssen equation is a classical theory for silo pressure calculations, proposed by the German engineer H. A. Janssen in 1895 (Janssen 1895; Sperl 2005). Based on the principle of static equilibrium, this theory describes the distribution of lateral pressure exerted by stored grain on silo walls (Hua and Feng 1994). As an accumulation of granular materials, sediments exert pressure on salt cavern walls through mechanisms similar to those encountered in silo problems: both materials exhibit discrete characteristics, and the geometry of salt caverns is similar to that of silos (Yuan et al. 2016). In fact, the Janssen equation has already been applied to the study of sediments. For example, Li et al. (2022) employed this theory to investigate the variation in sediment porosity with depth in cylindrical salt caverns. Although their study extensively investigated the restraining effect of sediments on salt cavern shrinkage, it did not focus on calculating the pressure exerted by sediments on cavern walls.

Based on practical engineering conditions, this study develops a Janssen-based formulation for calculating sediment pressure in salt caverns with different geometries, including cylindrical, conical, spherical, cylindrical–conical, and cylindrical–spherical caverns. The formulation is implemented in FLAC^{3D} and validated against a benchmark model based on coupled PFC^{3D}–FLAC^{3D} simulations. An engineering case study and parametric analyses are further conducted to examine the effects of cavern geometry, sediment accumulation height, cavern radius, and cavern-wall friction coefficient on sediment-pressure distribution and its contribution to cavern stability. The proposed formulation provides a computationally efficient approach for incorporating sediment pressure into numerical stability analyses of salt cavern gas storage.

2. Calculation method for sediment pressure

2.1 Simplification of cavern geometry and sediment morphology

Most salt deposits in China are exploited by continuous solution mining. During solution mining, the salt concentration and density of brine in contact with the dissolving rock salt surface increase as dissolution proceeds. The denser brine subsequently migrates downward under gravity-driven density segregation, resulting in pronounced vertical stratification of brine concentration within the cavern. Specifically, the upper part of the cavern contains relatively dilute brine and exhibits the highest rock salt dissolution rate, followed by dissolution along the cavern sidewalls. In contrast, the brine at the cavern bottom approaches saturation, resulting in the lowest dissolution rate. Consequently, the resulting salt caverns generally exhibit similar geometric characteristics, with an approximately arched roof, a nearly cylindrical middle section, and a spherical-cap-shaped or conical bottom (Wang 2003).

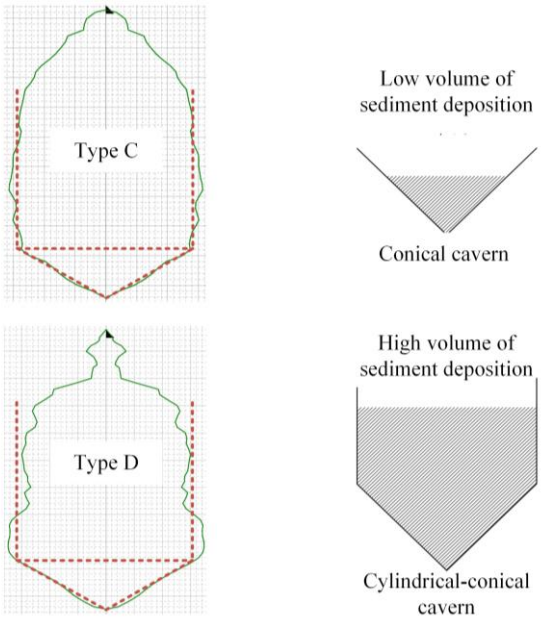


Fig. 2. Conical caverns based on sonar detection results of typical salt caverns

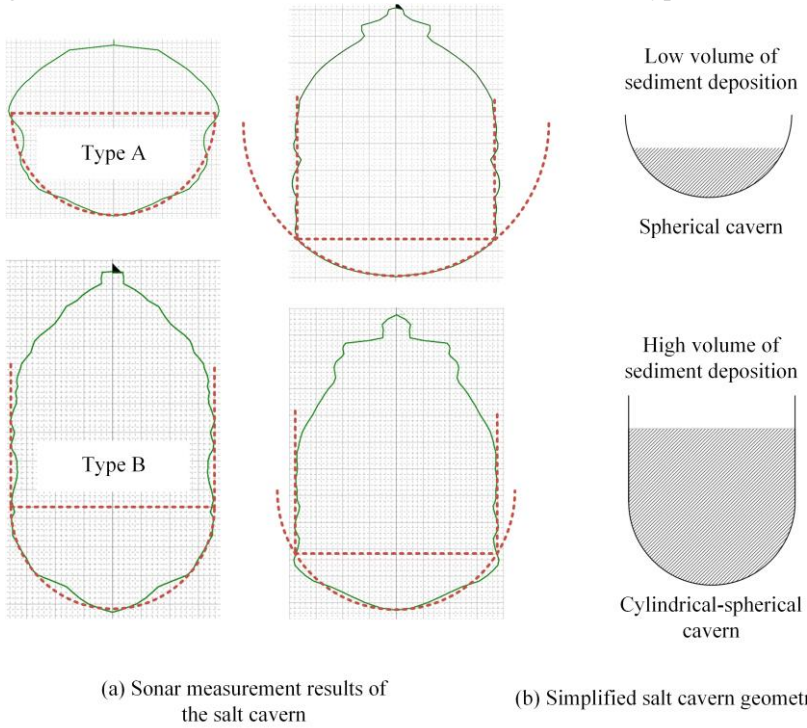


Fig. 3. Spherical caverns based on sonar detection results of typical salt caverns

Based on the cavern geometries obtained from sonar surveys of representative salt caverns in China and the spatial distribution characteristics of accumulated sediments, salt cavern geometries were simplified into two categories (Fig. 2 and Fig. 3): cylindrical–spherical caverns and cylindrical–conical caverns. When the sediment accumulation height is relatively low, the sediments are confined to the spherical-cap or conical bottom section. As the sediment accumulation height increases, the sediments extend into the middle cylindrical section.

The accumulated sediments mainly consist of two components. The first comprises fine particles or small rock fragments formed by the fragmentation and bulking of insoluble materials during the solution mining of bedded rock

salt (He et al. 2025). These particles may be transported to the surface with the discharged brine if they are located near the inlet of the brine production well (Sun et al. 2017). The second consists of large rock blocks formed by the instability and collapse of interlayers following the dissolution of the underlying rock salt (Shi et al. 2011; Hu et al. 2024). After dissolving bedded rock salt core samples, the residual sediments were oven-dried and sieved. The resulting particle size distribution is shown in Fig. 4.

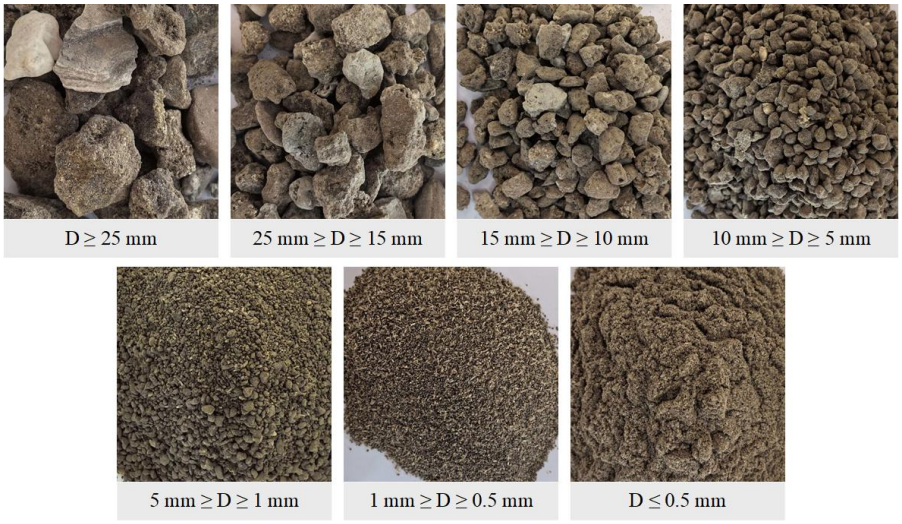


Fig. 4. Screening results of sediment samples

When assessing the stability of salt caverns containing sediments for gas storage, sediment pressure is commonly calculated using $p = \rho g h$. Although this method is widely used to estimate the in situ stress in undisturbed rock masses, it has certain limitations when applied to sediment pressure calculations. This is primarily because the equation does not account for the effects of actual cavern geometry and friction between the sediments and cavern walls on the pressure distribution. When the sediment accumulation height is relatively large or the cavern is located at a shallow depth, the resulting calculation errors may lead to inaccuracies in the stability assessment of salt cavern gas storage facilities (Fig. 5). Therefore, this study aims to improve the method for calculating sediment pressure based on the Janssen equation to more accurately represent the actual stress state of the sediments.

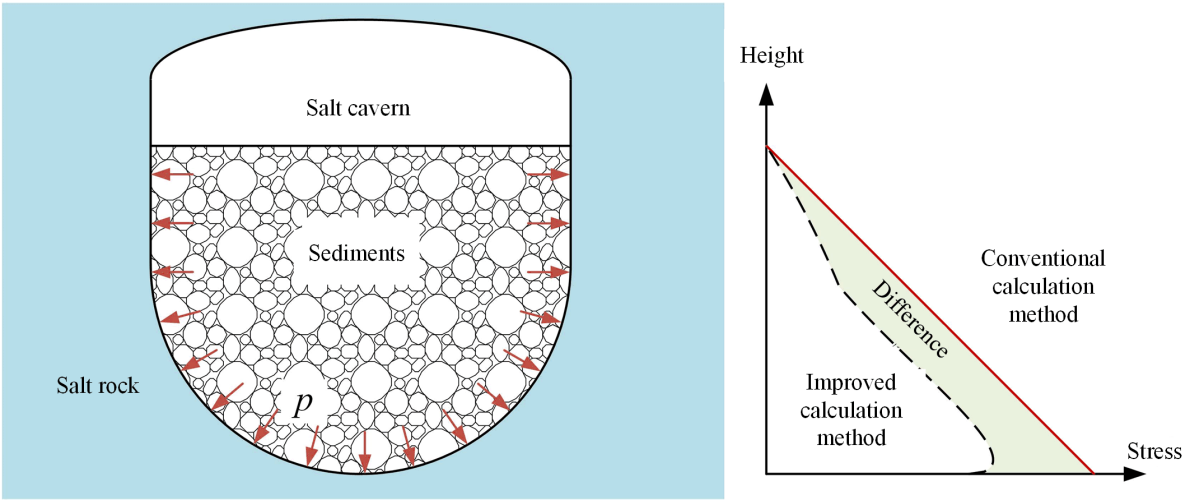


Fig. 5. Normal stress of sediment on cavern wall

2.2 Calculation method for the cylindrical cavern

The sediment pressure in the cylindrical section of the cavern can be calculated using the Janssen equation. Before conducting the mechanical analysis, the following assumptions are made (Chen and Zhu 1996):

(1) The vertical pressure is uniform at any given horizontal plane within the cavern and is proportional to the horizontal pressure, as expressed in Eq. (1),

$$p = kq \tag{1}$$

where p is the normal pressure exerted by the sediment layer on the cavern wall; k is the normal pressure coefficient, which depends on the inclination angle of the cavern wall; and q is the vertical pressure acting on the surface of the sediment layer.

(2) The sediment particles are assumed to be incompressible;

(3) The frictional force is proportional to the normal pressure exerted on the cavern wall, as expressed in Eq. (2),

$$f = \mu p \tag{2}$$

where f is the frictional force between the sediments and the cavern wall, and μ is the friction coefficient;

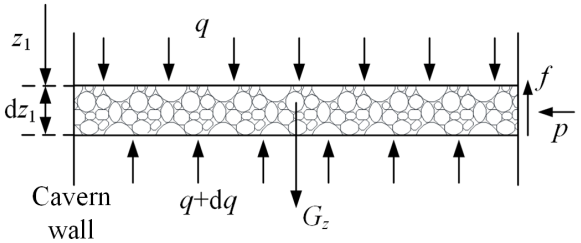


Fig. 6. Mechanical Model of Janssen's theory

The Janssen equation assumes an infinitely deep cylindrical silo. Accordingly, a downward-positive coordinate system is established with its origin at the top surface of the sediments. Based on the simplified mechanical model of a sediment micro-layer in the cylindrical cavern (see Fig. 6), the force equilibrium equation can be expressed as Eq. (3),

$$A_s \rho_s g \mathrm{d}z_1 + A_s q = A_s \left(q + \mathrm{d}q\right) + 2\frac{A_s}{R} f \mathrm{d}z_1 \tag{3}$$

where A_s is the area of the lower surface of the selected sediment micro-layer, ρ_s is the sediment density, and q is the vertical pressure acting on the upper surface of the sediment micro-layer.

Substituting Eqs. (1) and (2) into Eq. (3) and simplifying yields Eq. (4).

$$\rho_s g = \frac{\mathrm{d}q}{\mathrm{d}z_1} + \frac{2\mu k}{R} q \tag{4}$$

Substituting the solution into Eq. (1) gives the normal pressure exerted by the sediments on the cavern wall in the cylindrical section (Lei et al. 2019; Tang et al. 2021), as expressed in Eq. (5),

$$p = \frac{R\rho_s g}{2\mu}\left(1 - \mathrm{e}^{-\frac{2\mu k}{R} z_1}\right) \tag{5}$$

2.3 Calculation method for the conical cavern

For the conical cavern section, an upward-positive vertical coordinate system is established with its origin at the bottom of the cone (z = 0), where z increases upward along the height of the cavern. The inclination angle between the cavern wall and the horizontal plane is denoted by α_w. Assuming that the total sediment accumulation height is h_0, a sediment micro-layer with a thickness of dz is selected for force analysis, as illustrated in Fig. 7.

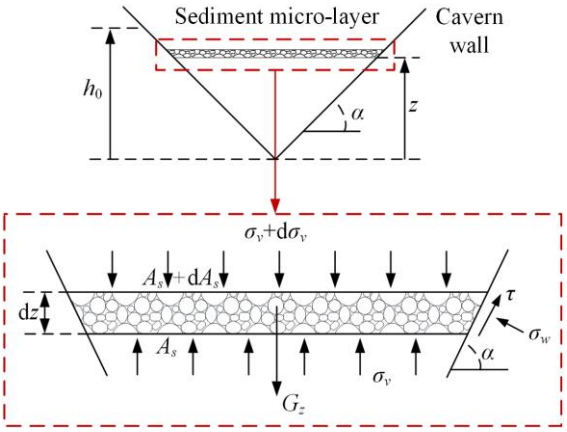


Fig. 7 Mechanical model of sediment micro-layer in conical cavern

Based on the vertical static equilibrium of the sediment micro-layer, the force equilibrium equation can be expressed as Eq. (6):

$$\frac{1}{3}\pi \mathrm{d}z\left[\left(\frac{z}{\tan\alpha_w}\right)^2+\left(\frac{z+\mathrm{d}z}{\tan\alpha_w}\right)^2+\frac{z\left(z+\mathrm{d}z\right)}{\tan^2\alpha_w}\right]\rho_s g+\left(A_s+\mathrm{d}A_s\right)\left(q+\mathrm{d}q\right)= A_s q+f\sin\alpha_w L_w\frac{\mathrm{d}z}{\sin\alpha_w}+p\cos\alpha_w L_w\frac{\mathrm{d}z}{\sin\alpha_w} \tag{6}$$

According to the geometric relationships of the conical cavern, the following expressions can be obtained as Eqs. (7) and (8):

$$L_w=2\pi\frac{z}{\tan\alpha_w} \tag{7}$$

$$A_s=\pi\frac{z^2}{\tan^2\alpha_w} \tag{8}$$

Substituting these geometric relationships into Eq. (6):

$$\frac{1}{3}\pi \mathrm{d}z\left[\left(\frac{z}{\tan\alpha_w}\right)^2+\left(\frac{z+\mathrm{d}z}{\tan\alpha_w}\right)^2+\frac{z}{\tan\alpha_w}\frac{z+\mathrm{d}z}{\tan\alpha_w}\right]\rho_s g +\left(\pi\frac{z^2}{\tan^2\alpha_w}+\frac{2\pi z}{\tan^2\alpha_w}\mathrm{d}z\right)\left(q+\mathrm{d}q\right)=\pi\frac{z^2}{\tan^2\alpha_w}q+\mu kq\frac{2\pi z\mathrm{d}z}{\tan\alpha_w}+kq\frac{2\pi z\mathrm{d}z}{\tan^2\alpha_w} \tag{9}$$

Expanding the equation, neglecting higher-order infinitesimal terms, and simplifying yields a first-order linear nonhomogeneous ordinary differential equation, as expressed in Eq. (10),

$$\frac{\mathrm{d}q}{\mathrm{d}z}+\frac{2}{z}\left[1-k\left(\tan\alpha_w\mu+1\right)\right]q=-\rho_s g \tag{10}$$

Applying the boundary condition at the top surface of the sediments in the conical cavern, where $z = h_0$ and the vertical pressure $q = q_0$, and solving the differential equation yield the expressions for the vertical sediment pressure, as given in Eqs. (11) and (12),

$$q=\left(\frac{h_0}{z}\right)^n\left(q_0+\rho_s g\frac{h_0}{n+1}\right)-\frac{z\rho_s g}{n+1} \tag{11}$$

$$n=2\left[1-k\left(1+\mu\tan\alpha\right)\right] \tag{12}$$

Combining these expressions with the lateral pressure relationship, the normal pressure exerted by the sediments on the cavern wall can be expressed as Eq. (13),

$$p = k\left[\left(\frac{h_0}{z}\right)^n\left(q_0 + \rho_s g\frac{h_0}{n+1}\right) - \frac{z\rho_s g}{n+1}\right] \tag{13}$$

2.4 Calculation method for the spherical cavern section

For the spherical cavern section, an upward-positive vertical coordinate system is established with its origin at the lowest point of the spherical cavern ($z = 0$), where z increases upward along the cavern height. The radius of the spherical cavern is denoted by R. A sediment micro-layer with a thickness of dz is selected for force analysis, as illustrated in Fig. 8.

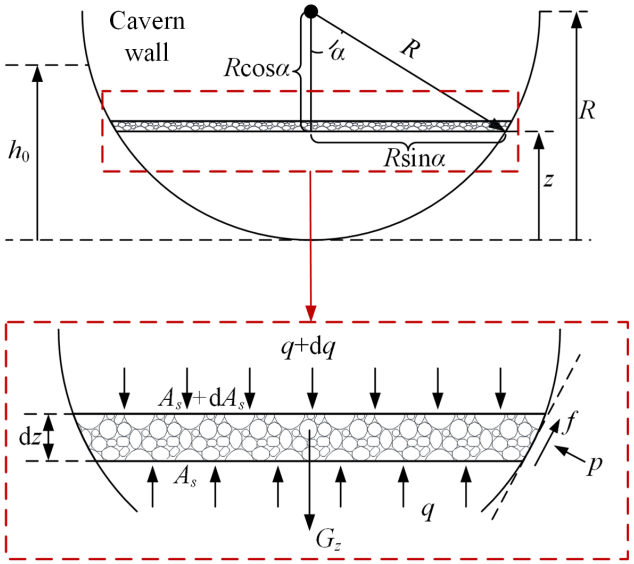


Fig. 8 Mechanical model of sediment micro-layer in spherical salt cavern

Based on the vertical static equilibrium of the sediment micro-layer, the force equilibrium equation can be expressed as Eq. (14),

$$\begin{aligned}&\frac{2A_s + \mathrm{d}A_s + \mathrm{d}^2 z}{2}\rho_s g\mathrm{d}z + \left(A_s + \mathrm{d}A_s\right)\left(q + \mathrm{d}q\right) = \\ &A_s q + f\sin\alpha L_w\frac{\mathrm{d}z}{\sin\alpha_w} + p\cos\alpha L_w\frac{\mathrm{d}z}{\sin\alpha_w}\end{aligned} \tag{14}$$

According to the geometric relationships of the spherical cavern, Eqs. (15) – (19) can be obtained,

$$L_w = 2\pi R\sin\alpha_w \tag{15}$$

$$A_s = \pi R^2\sin^2\alpha_w \tag{16}$$

$$\sin\alpha_w = \frac{\sqrt{2Rz - z^2}}{R} \tag{17}$$

$$\cos\alpha_w = \frac{R - z}{R} \tag{18}$$

$$\cot\alpha = \frac{R - z}{\sqrt{2Rz - z^2}} \tag{19}$$

Unlike the cylindrical and conical cavern sections, the wall inclination angle of the spherical cavern varies continuously with depth z. Consequently, the lateral pressure coefficient k also varies with depth and is denoted by $k(z)$. Generally, the normal pressure coefficient can be determined through uniaxial

compression tests, with values typically ranging from 0.4 to 0.6 for vertical cavern walls (Saleh et al. 2018). At the top of the spherical cavern ($z = R$), where the cavern wall is vertical, $k(z)|_{z=R} = 0.5$ is adopted in this study. At the bottom of the spherical cavern ($z = 0$), where the cavern wall is horizontal, the vertical sediment pressure is equal to the normal pressure acting on the cavern wall, and thus $k(z)|_{z=0} = 1$ is adopted.

Walters (1973) has investigated the relationship between the normal pressure coefficient and the inclination angle of silo walls. However, their methods for determining this coefficient are relatively complex, making them inconvenient for the subsequent analytical derivation in this study. Therefore, to simplify the subsequent analytical derivation while maintaining computational feasibility, a linear relationship is proposed to describe the variation in the lateral pressure coefficient with depth, as expressed in Eq. (20) (Fig. 9):

$$k(z) = 1 - \frac{z}{2R} \tag{20}$$

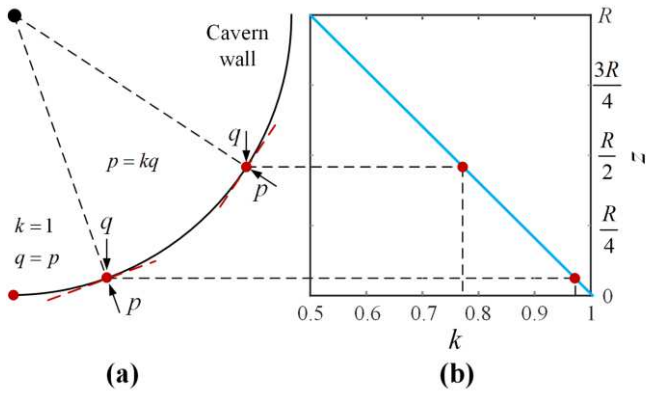


Fig. 9. Value law of lateral pressure coefficient

This linear expression satisfies the boundary conditions of $k = 1$ at $z = 0$ and $k = 0.5$ at $z = R$, while maintaining consistency with the lateral pressure coefficient adopted for the conical cavern section. By incorporating the geometric relationship between the wall inclination angle α_w and z, an expression for the lateral pressure coefficient applicable to cavern walls with arbitrary inclination angles can be derived, as given in Eq. (21),

$$k(\alpha_w) = \frac{1 + \cos\alpha_w}{2} \tag{21}$$

Substituting Eqs. (1), (2), and (15) – (19) into Eq. (14), expanding the resulting equation, and neglecting higher-order infinitesimal terms yields a first-order linear nonhomogeneous ordinary differential equation, as expressed in Eq. (22),

$$\frac{\mathrm{d}q}{\mathrm{d}z} + 2\frac{R - z - \left(1 - \frac{z}{2R}\right)\left(\mu\sqrt{2Rz - z^2} + R - z\right)}{z(2R - z)}q = -\rho_s g \tag{22}$$

The general solution of this differential equation is given in Eq. (23),

$$q = \mathrm{e}^{-\int u(z)\mathrm{d}z}\left(\int v(z)\mathrm{e}^{\int u(z)\mathrm{d}z}\mathrm{d}z + C_1\right) \tag{23}$$

where the coefficient term and the nonhomogeneous term are expressed by Eqs. (24) and (25), respectively.

$$u(z)=2\frac{R-z-\left(1-\frac{z}{2R}\right)\left(\mu\sqrt{2Rz-z^2}+R-z\right)}{z\left(2R-z\right)} \tag{24}$$

208

$$v(z)=-\rho_s g \tag{25}$$

209 Integrating $u(z)$ yields Eq. (26).

$$\begin{aligned}\int u(z)\mathrm{d}z &= 2\int\frac{R-z-k\left(\mu\sqrt{2Rz-z^2}+R-z\right)}{z\left(2R-z\right)}\mathrm{d}z \\ &= \ln(2R-z)-2\mu\arcsin\sqrt{\frac{z}{2R}}-\frac{\mu}{R}\sqrt{2Rz-z^2}+\frac{z}{R}\end{aligned} \tag{26}$$

210 Analytical derivation confirms that the indefinite integral $\int \mathrm{e}^{\int u(z)\mathrm{d}z}\mathrm{d}z$ cannot be expressed in terms of

211 elementary functions. Therefore, an approximate function-fitting method is adopted to evaluate the integral.

212 Denoting the exact integral result as $I(z)$ and its approximation as $\mathrm{I}_{app}(z)$, the corresponding expressions are

213 given in Eq. (27),

$$\begin{aligned}I\left(z\right) &= \ln(2R-z)-2\mu\arcsin\sqrt{\frac{z}{2R}}-\frac{\mu}{R}\sqrt{2Rz-z^2}+\frac{z}{R}\approx \\ I_{app}\left(z\right) &= C_2-2\mu\sqrt{\frac{z}{2R}}\end{aligned} \tag{27}$$

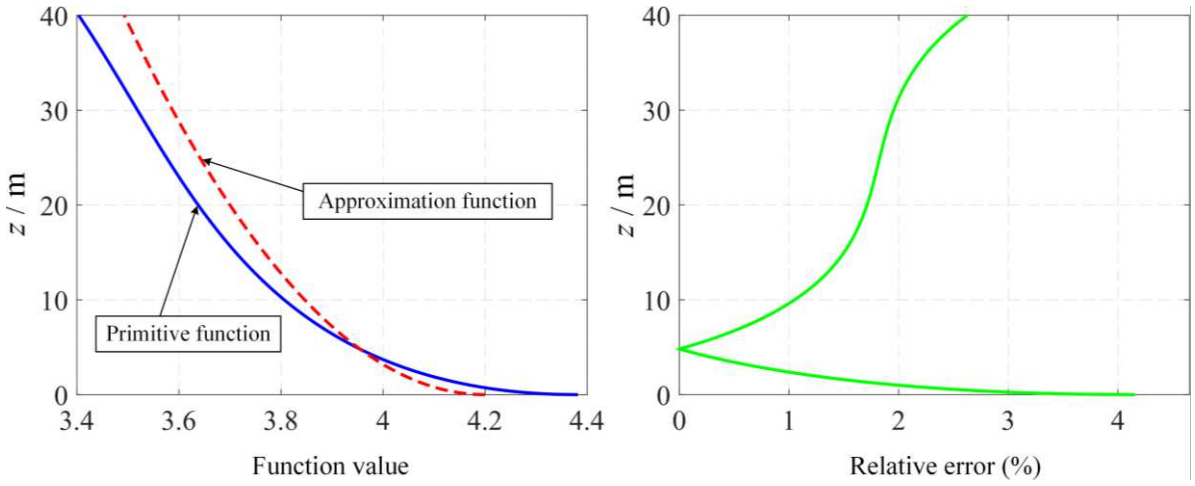
214 Taking representative engineering parameters of $\mu = 0.5$ and $R = 40$ m as an example, with $C_2 = 4.1$, the

215 error between the approximate function and the original expression remains within 4%, satisfying the

216 requirements for engineering calculations, as shown in Fig. 10. It should be noted that the constant term C_2

217 cancels out during the subsequent derivation and therefore introduces no additional error into the final

218 pressure calculation, ensuring the reliability of the approximation method.



219

220 Fig. 10. Fitting results and error of approximate function for integral term

221 Substituting the approximate expression into the general solution yields Eq. (28).

$$\begin{aligned}\int \mathrm{e}^{\int u(z)\mathrm{d}z}\mathrm{d}z &= \int \mathrm{e}^{C_2-2\mu\sqrt{\frac{z}{2R}}}\mathrm{d}z \\ &= -\frac{R}{\mu^2}\left(2\mu\sqrt{\frac{z}{2R}}+1\right)\mathrm{e}^{C_2-2\mu\sqrt{\frac{z}{2R}}}\end{aligned} \tag{28}$$

Substituting Eq. (28) into Eq. (23) gives Eq. (29),

$$q = \rho g \frac{\mu\sqrt{2Rz} + R}{\mu^2} + C_1 \mathrm{e}^{-2\mu\sqrt{\frac{z}{2R}}} \tag{29}$$

Applying the boundary condition at the top surface of the sediments in the spherical cavern, where $z = h_0$ and the vertical pressure $q = q_0$, the integration constant C_1 can be determined, as given in Eq. (30),

$$C_1 = \left(q_0 - \rho g \frac{\mu\sqrt{2Rh_0} + R}{\mu^2} \right) \mathrm{e}^{-2\mu\sqrt{\frac{h_0}{2R}}} \tag{30}$$

Substituting C_1 back into Eq. (29) yields the final expression for the vertical sediment pressure distribution in the spherical cavern, as given in Eq. (31),

$$q = \rho_s g \frac{\mu\sqrt{2Rz} + R}{\mu^2} + \left(q_0 - \rho_s g \frac{\mu\sqrt{2Rh_0} + R}{\mu^2} \right) \mathrm{e}^{\frac{2\mu}{\sqrt{2R}}\left(\sqrt{z} - \sqrt{h_0}\right)} \tag{31}$$

Combining this expression with the lateral pressure coefficient $k(z)$ gives the normal pressure exerted by the sediments on the cavern wall, as expressed in Eq. (32),

$$p = \left(1 - \frac{z}{2R}\right) \left[\rho_s g \frac{\mu\sqrt{2Rz} + R}{\mu^2} + \left(q_0 - \rho_s g \frac{\mu\sqrt{2Rh_0} + R}{\mu^2} \right) \mathrm{e}^{\frac{2\mu}{\sqrt{2R}}\left(\sqrt{z} - \sqrt{h_0}\right)} \right] \tag{32}$$

2.5 Calculation method for the cylindrical–conical and cylindrical–spherical caverns

As discussed previously based on the sonar survey results, salt caverns encountered in engineering practice predominantly exhibit combined cylindrical–conical or cylindrical–spherical geometries. Since the coordinate systems adopted for the cylindrical, conical, and spherical sections have different origins and axis directions in the theoretical calculations, the coordinate systems must first be unified before performing piecewise calculations. Meanwhile, the vertical pressure at the bottom of the cylindrical section is taken as the overlying boundary load q_0 acting on the top of the conical or spherical section.

The coordinate systems are unified as follows: the origin is set at the lowest point of the cavern ($z = 0$), with z increasing upward along the cavern height. Let h_1 denote the total height of the combined cavern, and let $z = h_0$ denote the elevation of the interface between the cylindrical section and the conical or spherical section. For the cylindrical section, $z \in [h_0, h_1]$, corresponding to $z_1 = h_1 - z$ in the original cylindrical coordinate system. For the conical and spherical sections, $z \in [0, h_0]$, and the coordinate systems remain consistent with those defined previously.

(1) Cylindrical–conical cavern

After transforming the coordinates of the cylindrical section, the normal pressure exerted by the sediments on the cavern wall in this section can be calculated using Eq. (5). For the conical section, Eq. (11) is adopted, where the overlying boundary load q_0 at the top of the conical section is determined by the vertical pressure at the bottom of the cylindrical section ($z = h_0$). Accordingly, the piecewise formula for calculating the normal pressure exerted by the sediments on the cavern wall in the combined cylindrical–conical cavern is obtained as Eqs. (33), (34) and (35):

$$\begin{cases} p = \dfrac{R\rho_s g}{2\mu}\left(1-\mathrm{e}^{-\frac{2\mu k}{R}(h_1-z)}\right) & z \geq h_0 \\ p = k\left(\dfrac{h_0}{z}\right)^n\left(q_0+\rho_s g\dfrac{h_0}{n+1}\right)-\dfrac{z\rho_s g}{n+1} & z \leq h_0 \end{cases} \tag{33}$$

$$n = 2\left[1-k\left(1+\mu\tan\alpha\right)\right] \tag{34}$$

$$q_0 = \frac{R\rho_s g}{2\mu k}\left(1-\mathrm{e}^{-\frac{2\mu k}{R}(h_1-h_0)}\right) \tag{35}$$

(2) Cylindrical–spherical cavern

Similarly, the piecewise formulas for calculating the normal pressure exerted by the sediments on the cavern wall in the combined cylindrical–spherical cavern are obtained, as given in Eqs. (36) and (37),

$$\begin{cases} p = \dfrac{R\rho g}{2\mu}\left(1-\mathrm{e}^{-\frac{2\mu k}{R}(h_1-z)}\right) & z \geq h_0 \\ p = \left(1-\dfrac{z}{2R}\right)\left[\rho g\dfrac{\mu\sqrt{2Rz}+R}{\mu^2}+\left(q_0-\rho g\dfrac{\mu\sqrt{2Rh_0}+R}{\mu^2}\right)\mathrm{e}^{\frac{2\mu}{\sqrt{2R}}\left(\sqrt{z}-\sqrt{h_0}\right)}\right] & z \leq h_0 \end{cases} \tag{36}$$

$$q_0 = \frac{R\rho g}{2\mu k}\left(1-\mathrm{e}^{-\frac{2\mu k}{R}(h_1-h_0)}\right) \tag{37}$$

Based on the above piecewise formulas, the distribution of the normal pressure exerted by the sediments on the cavern walls over the entire cavern depth can be calculated for salt caverns with different combined geometries, as shown in Fig. 11.

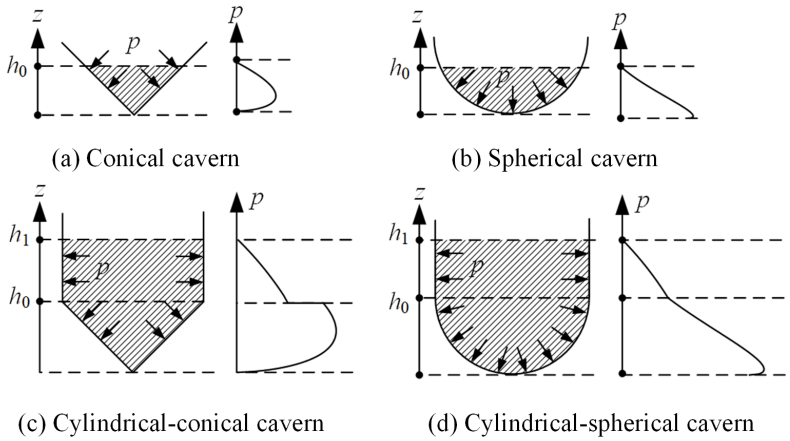


Fig. 11. Distribution characteristics of normal pressure of sediment in typical caverns

3 Verification of the calculation method

3.1 Validation method

Numerical simulation is currently the primary method for assessing the stability of salt cavern gas storage facilities. In this study, a comparative approach involving two numerical models was adopted to validate the accuracy of the proposed sediment pressure calculation method. The PFC^{3D}–FLAC^{3D} coupled numerical simulation was employed as the benchmark model, while the proposed calculation method was

implemented in FLAC^{3D} to establish the validation model. Both models were simulated under identical operating conditions, and the proposed method was validated by comparing their results.

(1) Benchmark model

FLAC^{3D} is a finite difference software package widely used in stability studies of salt cavern gas storage facilities, whereas PFC^{3D} is a discrete element software package capable of simulating the mechanical behavior of granular geomaterials. In the PFC^{3D}–FLAC^{3D} coupled benchmark model, the sediments are represented as discrete particles, while the surrounding rock mass is treated as a continuum. Coupling is achieved by establishing an interface along the cavern wall that enables information exchange between the two domains. Changes in forces and velocities induced by rock creep or sediment particle movement are transferred through this interface, thereby achieving numerical coupling. This model enables accurate simulation and stability analysis of salt cavern gas storage facilities containing sediments.

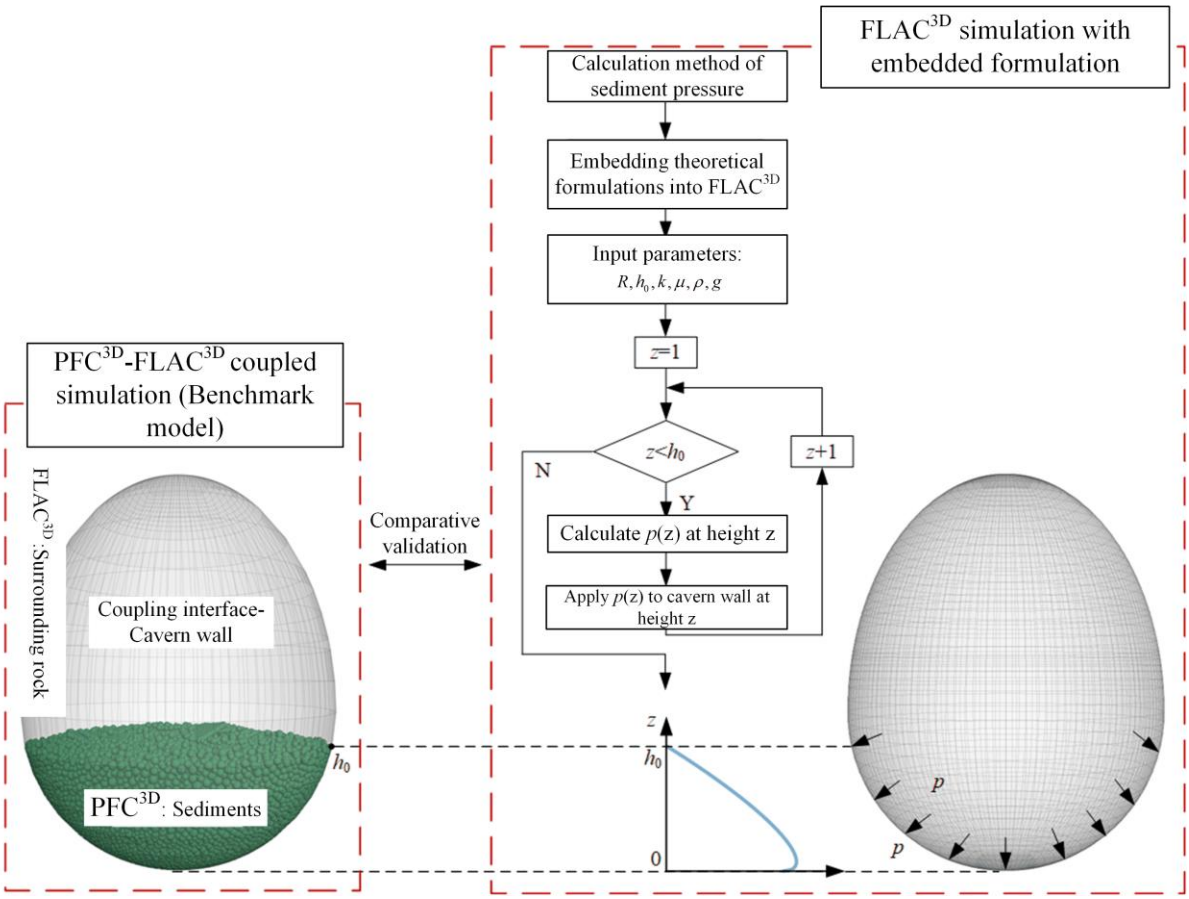


Fig. 12. Validation methodology and implementation workflow

(2) Validation model

The validation model was established by incorporating the proposed sediment pressure calculation formulas into FLAC^{3D}. First, the calculation formulas and the associated sediment parameters were defined using the built-in Fish functions in FLAC^{3D}. The depth variable z was then iterated from the bottom to the top of the sediments to calculate the corresponding cavern wall pressure $p(z)$ at each depth. Finally, the calculated pressure values were applied to the cavern walls as normal stress boundary conditions.

The corresponding parameters in the two models, including cavern geometry, sediment parameters, and boundary conditions, were kept identical. The primary difference between the models lies in how sediment pressure is represented. In the benchmark model, sediment pressure is simulated by generating discrete particles, providing greater accuracy and reliability. In contrast, the validation model implements the proposed calculation formulas

directly, offering higher computational efficiency. The validation procedure is illustrated in Fig. 12.

It should be emphasized that PFC^{3D}–FLAC^{3D} coupled simulations generally require substantial computational resources and long computation times when dealing with complex models. By incorporating the proposed calculation method into FLAC$_{3D}$, the simulation time can be significantly reduced, enabling more efficient stability analysis of salt cavern gas storage facilities. Taking the model described in the following section as an example, each PFC^{3D}–FLAC^{3D} coupled simulation case required approximately one month of computation on a workstation equipped with an 8-core, 16-thread CPU, whereas the FLAC^{3D} model incorporating the proposed calculation formulas required only approximately four days.

3.2 Parameter settings

(1) FLAC^{3D} model parameters

Considering the approximately annular distribution patterns observed in cross-sections of underground salt caverns, where the stress field, plastic zones, and displacement contours also exhibit annular distributions, and based on previous numerical simulations conducted by our research group indicating that rectangular model boundaries may affect the simulation results for pear-shaped caverns, a cylindrical computational model was established in this study, as shown in Fig. 13.

The model has a radius of 300 m and a height of 300 m. The upper half of the cavern is a semi-ellipsoid with three axis lengths of 40 m, 40 m, and 60 m, while the lower half is a hemisphere with a radius of 40 m. The top and bottom boundaries of the model are located at depths of 820 m and 1120 m, respectively, whereas the cavern roof and bottom are located at depths of 940 m and 1040 m, respectively.

The entire model was discretized using hexahedral elements, with a finer mesh near the cavern and a coarser mesh near the model boundaries. The boundary conditions were specified as follows: a vertically downward gravitational load representing the overlying rock mass was applied to the top boundary, with an average rock density of 2.3×10^3 kg/m^3; normal displacement constraints were imposed on the lateral and bottom boundaries; and the gravitational acceleration was set to 9.8 m/s^2. The creep parameters of rock salt were set to $A = 9.8 \times 10^{-5}$/y^{-1} and $n = 3.5$, while the remaining mechanical parameters of the rock mass are listed in Table 1 (Zhang et al. 2021b).

Considering the high internal connectivity of the sediments, which allows gas to move freely through the pore space, a constant gas pressure of 10 MPa was applied to all cavern wall surfaces, including those covered by accumulated sediments.

Table 1 Parameters in FLAC^{3D}

Lithology	E (GPa)	μ_1	c (MPa)	φ (°)	σ_t (MPa)
Interlayer	10.0	0.23	4.0	35	3.6
Salt rock	5.16	0.31	2.0	35	1.0

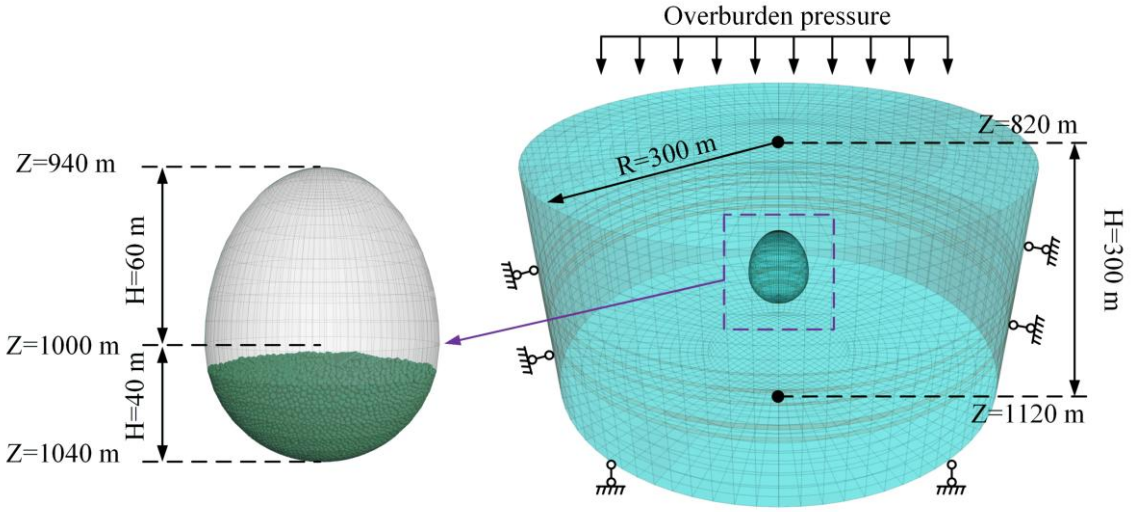


Fig. 13. Cavern model in FLAC^{3D}

(2) PFC^{3D} model parameters

Considering computational efficiency, it is impractical to generate particles that accurately reproduce the actual sizes and quantities of the sediments. Previous studies (Bo et al. 2022; Liu et al. 2009; Gu et al. 2017) have shown that, for underground engineering applications, size effects can be neglected when the overall dimensions of the particle-flow model exceed 10–30 times the mean particle diameter. Therefore, in this study, smaller insoluble fragments were represented by spherical particles (balls) with radii ranging from 0.5 to 1 m, whereas larger rock blocks were modeled as rigid clumps, including square and triangular blocks with side lengths of 2–10 m and thicknesses of 1–2 m. The corresponding model parameters are listed in Table 2 (Liu et al. 2024), where f_1 is the friction coefficient and n_1 is the damping coefficient.

Table 2 Parameters in PFC^{3D}

Sediment type	Radius/side length (m)	ρ (kg/m^3)	E (GPa)	f_1	n_1
Ball	0.5~1.0	2450	10	0.5	0.7
Clump	2~10	2450	10	0.5	0.7

Based on the geological characteristics of typical salt deposits in China, sediments in the high-grade Jintan salt mine predominantly consist of fine particles formed by the fragmentation and bulking of mudstone (Wanyan et al. 2015; Fan et al. 2025). In contrast, sediments in the medium-grade Yunying and Huai'an salt mines are characterized by a mixture of particles and rock blocks (Zeng et al., 2025), whereas those in the low-grade Pingdingshan, Zhangshu, and Kunming salt mines are dominated by large rock blocks.

Accordingly, three simulation cases were established (Table 3 and Fig. 14). In Case 1, the interlayer content was 20%, and the sediments consisted of 80% particles and 20% rock blocks. In Case 2, the interlayer content was 40%, with sediments comprising 60% particles and 40% rock blocks. In Case 3, the interlayer content was 60%, and the sediments consisted of 40% particles and 60% rock blocks.

Table 3 Sediment proportion of three cases

Grade	Interlayer volume fraction in the cavern	Proportion of insoluble particles	Proportion of insoluble rock blocks	Representative salt mine
High	20%	80%	20%	Jintan
Medium	40%	60%	40%	Huai'an
Low	60%	40%	60%	Tai'an

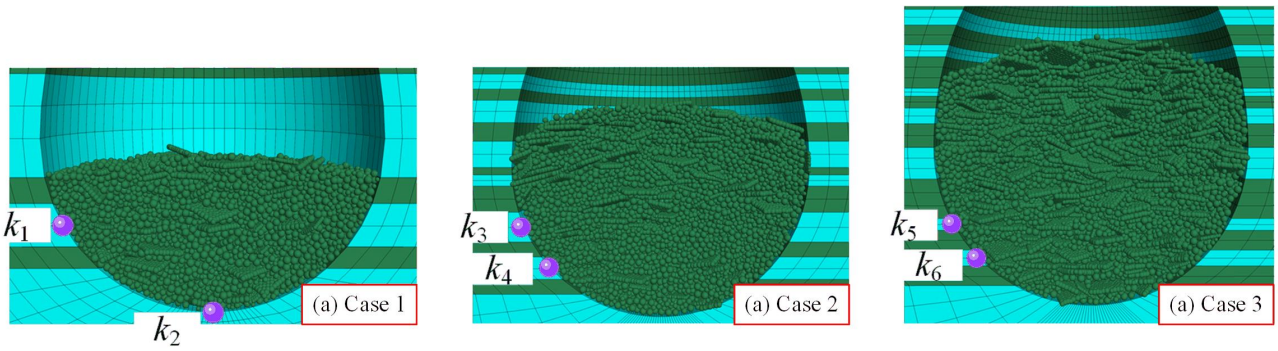


Fig. 14. Three cases and corresponding monitoring points

Sediments with corresponding accumulation heights were generated based on the total volume of collapsed interlayers. In Case 1, the sediment accumulation height was approximately 35 m, and monitoring points k_1 (approximately 14 m below the sediment surface) and k_2 (35 m below the sediment surface) were established. In Case 2, the sediment accumulation height was approximately 56 m, with monitoring points k_3 and k_4 located at depths of 28 m and 39 m below the sediment surface, respectively. In Case 3, the sediment accumulation height was approximately 62 m, with monitoring points k_5 and k_6 located at depths of 41 m and 50 m below the sediment surface, respectively. All monitoring points were located in the middle of the salt layer, where the displacement response was pronounced. The accuracy of the proposed pressure calculation method was validated by comparing the displacements at monitoring points located at different depths.

3.3 Validation results and error analysis

After 30 years of operation under the three simulation cases, the normal sediment pressures calculated using the improved method were compared with those obtained from the measurement spheres in the coupled model, as shown in Fig. 15. It can be observed that the sediment pressures calculated using the proposed method exhibit trends generally consistent with those obtained from the coupled simulations, with a maximum error of approximately 0.03 MPa. The errors in the middle and lower regions of the sediments are larger than those in the upper region.

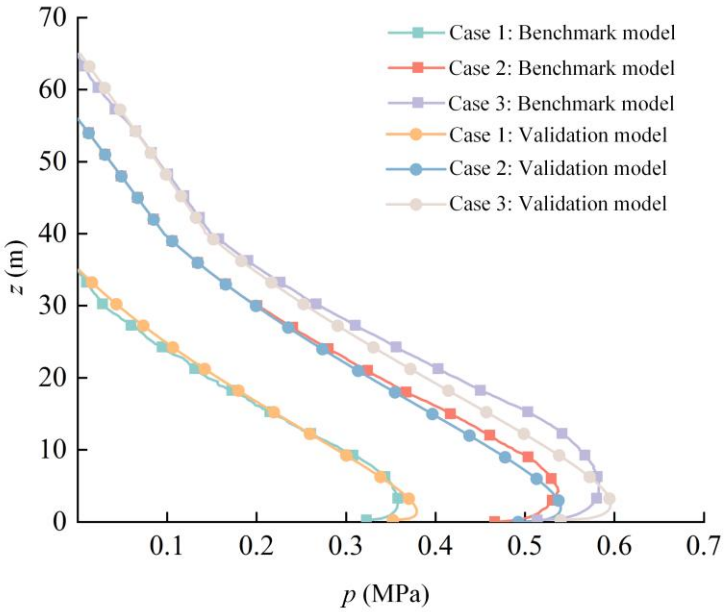


Fig. 15. Comparison of sediment pressure between analytical solution and coupling simulation

The errors may mainly arise from limitations in the statistical representativeness of the measurement spheres

(Fig. 16). The reliability of the results obtained from measurement spheres depends on satisfying the minimum sample size requirement for a representative volume element (RVE). Specifically, each measurement sphere must contain sufficient particles and effective contacts to eliminate random fluctuations in the discrete particle system. For broadly graded sediment materials, at least 50 effective particles are generally required within each measurement sphere, whereas a minimum of 30 particles is required for uniformly sized particle systems. Below these thresholds, the variability of the calculated stress statistics increases significantly.

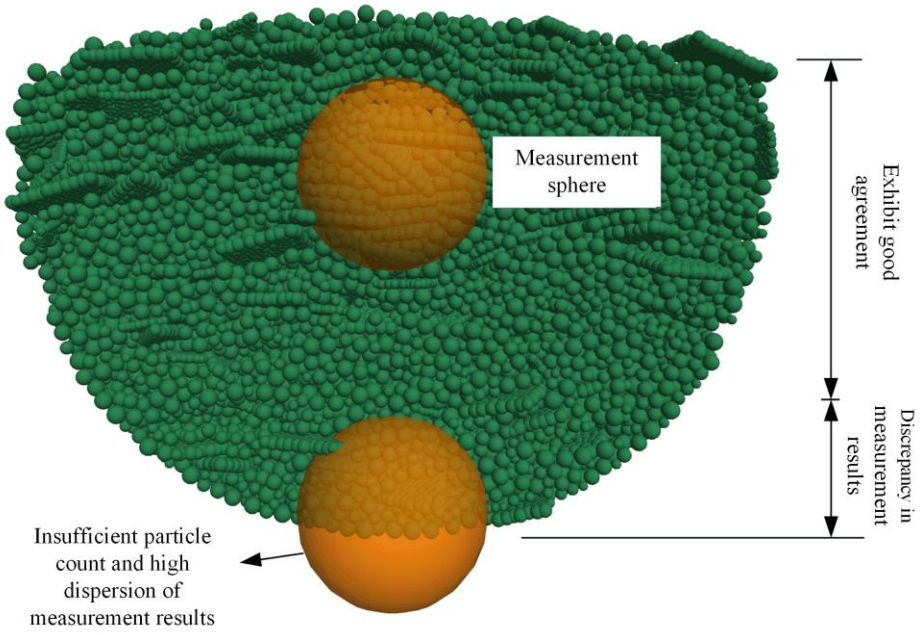


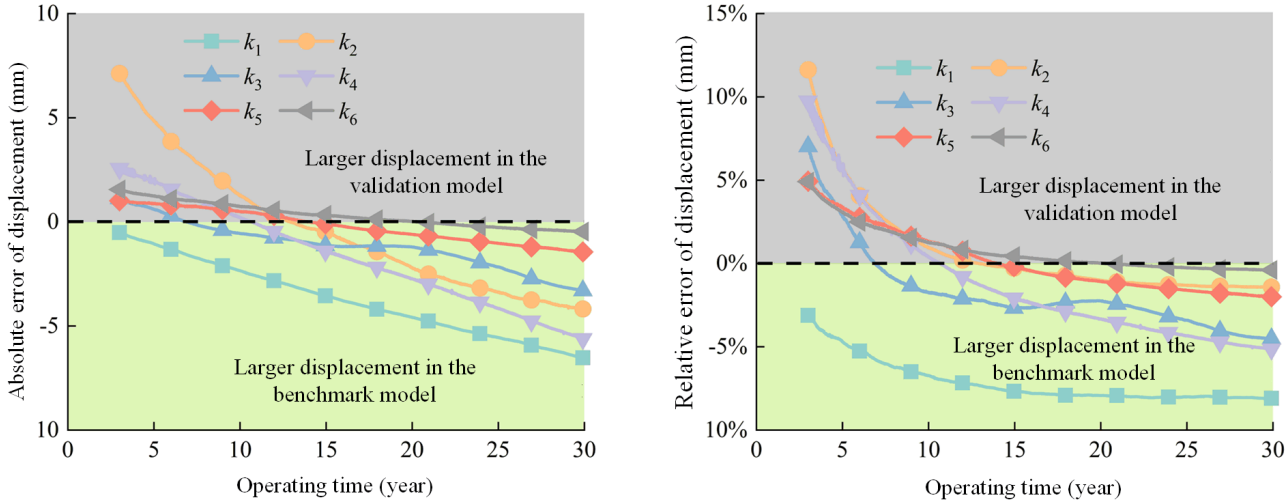
Fig. 16. Layout of measuring sphere

In the upper sediment region, the measurement spheres can be entirely contained within the sediments, and the number of effective particles satisfies the RVE requirements, resulting in stable statistical results. However, near the cavern bottom, the constricted geometric boundaries reduce the effective sampling volume of the measurement spheres, causing the number of effective particles within them to fall substantially below the required threshold and consequently increasing the variability of the statistical results.

Since the calculation procedure of the measurement spheres may introduce certain errors, the displacement results at six monitoring points were further compared between the two models. The absolute error was defined as the difference between the displacement calculated by the validation model and that calculated by the benchmark model (Fig. 17(a)), while the relative error was defined as the absolute error divided by the displacement calculated by the benchmark model, expressed as a percentage (Fig. 17(b)).

The error curves indicate that, throughout the 30-year operation period, the absolute displacement errors at all monitoring points remained generally within ±5 mm, while the relative errors did not exceed ±5%, confirming the reliability of the proposed sediment pressure calculation method. These results demonstrate that incorporating the proposed calculation method into FLAC^{3D} can effectively replace computationally intensive PFC^{3D}–FLAC^{3D} coupled simulations within acceptable engineering accuracy, particularly for high-impurity salt deposits containing large

quantities of sediment particles and large-scale cavern groups in salt formations containing impurities.



(a) Absolute error of the monitoring points (b) Relative error of the monitoring points

Fig. 17. Evolution law of absolute and relative displacement error of monitoring points

Meanwhile, a distinct time-dependent trend was observed. During the initial operation period, the displacements predicted by the validation model were generally larger than those obtained from the benchmark model (error > 0). As the operation time increased, the differences between the two models gradually decreased, and eventually, the displacements predicted by the validation model became smaller than those obtained from the benchmark model (error < 0). This behavior can be attributed to the fact that the proposed analytical method is based on static equilibrium and does not account for the dynamic evolution of sediment pressure caused by particle compression, rearrangement, and pore compaction during the long-term creep-induced shrinkage of salt caverns. Furthermore, the progressive creep deformation of the cavern alters the contact conditions between the sediments and cavern walls, whereas the analytical method assumes a fixed initial cavern geometry.

Regarding the differences among the three simulation cases, Case 1 exhibited the largest errors, while Case 3 showed the smallest. This is because a lower sediment content results in more pronounced creep-induced cavern shrinkage and greater changes in cavern geometry over time, leading to slightly larger deviations between the assumptions of the static analytical method and the actual operating conditions. Nevertheless, the overall errors remained within acceptable engineering limits.

4 Engineering case study and analysis of key parameter effects

4.1 Case study of a high sediment content salt mine in Huai'an

A salt cavern in a high-impurity salt mine in Huai'an was selected as an engineering case for sediment pressure analysis. The cavern is located at depths ranging from 1000 to 1250 m and exhibits a cylindrical–spherical geometry, with a sediment accumulation height of 200 m. The bulk density of the sediments, including pore space, is 1.4 g/cm³ (sediment solid density of 2.45 g/cm³ and porosity of 43%). The minimum operating pressure within the cavern is 8.5 MPa. The distribution of normal pressure exerted by the sediments on the cavern wall, calculated using the proposed method, is shown in Figs. 18 and 19.

The calculation results indicate that, in the cylindrical section, the normal pressure exerted by the sediments on the cavern wall increases progressively with depth from the sediment surface, while its rate of increase gradually decreases, reaching 0.64 MPa at the interface between the cylindrical and spherical sections. In the spherical section, the rate of pressure increase rises significantly, with the pressure reaching a maximum of 1.31 MPa near the cavern bottom before decreasing within a very small region at the lowest point of the cavern. Under the minimum operating

pressure condition, the sediment pressure increases the total pressure acting on the cavern wall to 9.81 MPa, representing a 15.4% increase relative to the operating pressure and effectively improving the stress state of the cavern wall.

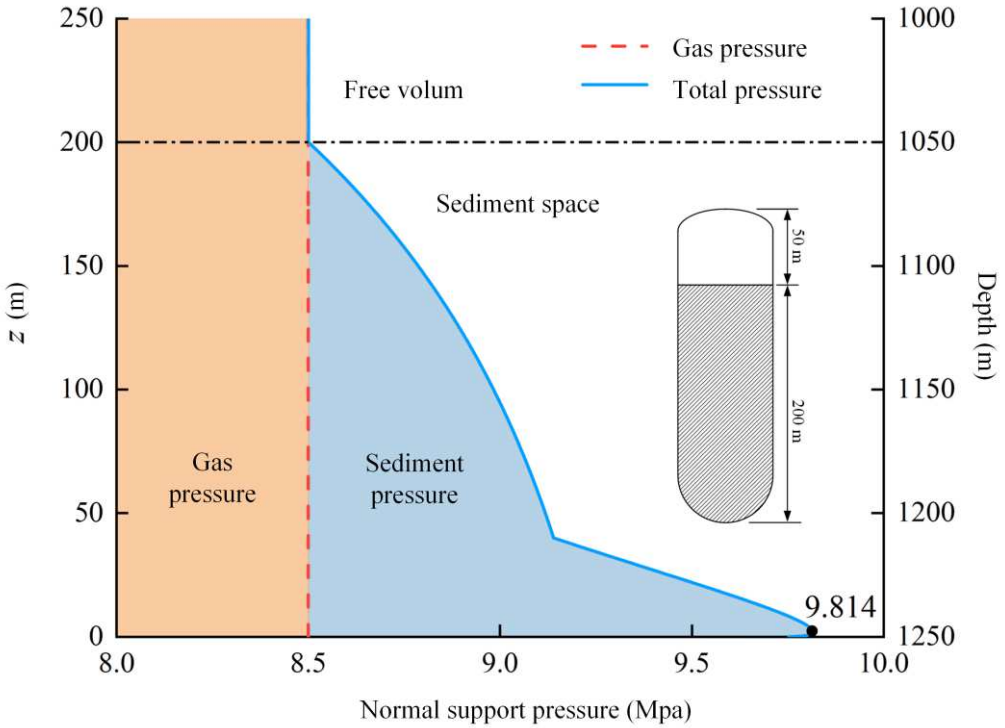


Fig. 18. Total pressure in caverns with high sediment content

The gas pressure within a salt cavern is uniform along the cavern walls. Therefore, in the absence of sediments, the cavern bottom, which is located at the greatest burial depth and subjected to the highest in situ stress, exhibits the lowest ratio of internal pressure to in situ stress, making it the most critical region for stability control. At the minimum operating pressure of 8.5 MPa, the ratio of internal pressure to in situ stress is 37.7% at the cavern roof, but only 30.1% at the cavern bottom. With the supporting effect of the sediments, the ratio of total pressure to in situ stress at the cavern bottom increases significantly from 30.1% to 34.6%. Moreover, the minimum pressure-to-in situ stress ratio throughout the entire cavern increases to 33.5%. These results clearly demonstrate that, in high-impurity salt deposits, the pressure exerted by sediments can effectively supplement the supporting pressure acting on the cavern walls, significantly enhancing the overall stability of salt cavern gas storage facilities, particularly during periods of minimum operating pressure. In practical engineering applications, when the sediment thickness and physical properties are known, the minimum operating pressure can be appropriately reduced, thereby increasing the working gas capacity.

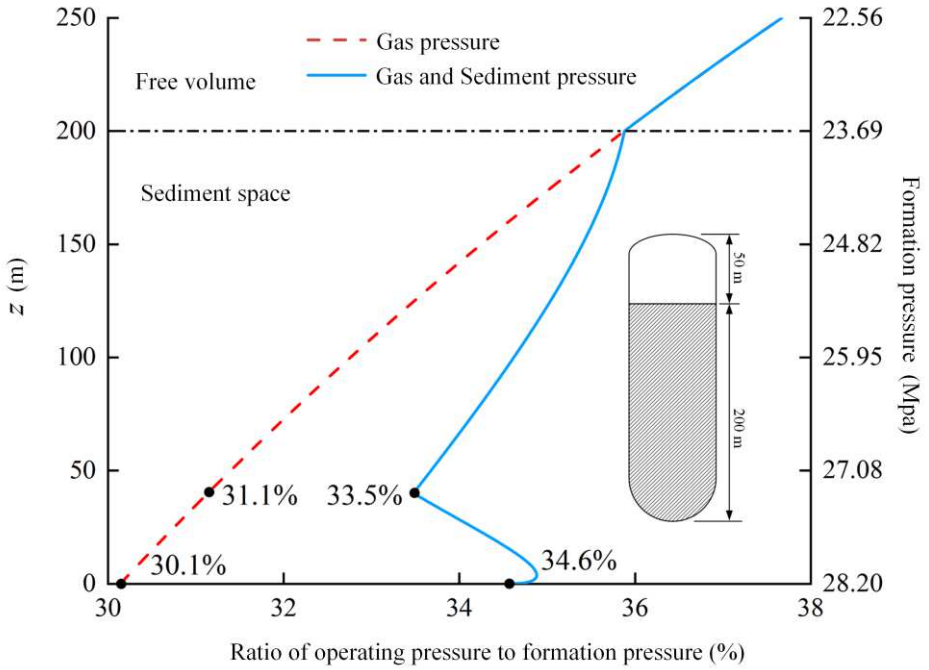


Fig. 19. Ratio of total pressure in cavern with high sediment content to in-situ stress

4.2 Analysis of key parameter effects

4.2.1 Cavern geometry

To investigate sediment pressure in caverns with different geometries, the sediment accumulation height was fixed at 40 m, while the remaining parameters were kept identical to those in the engineering case study. The hydrostatic pressure equation and the calculation method proposed in this study were applied to determine the distributions of vertical sediment pressure and normal pressure exerted by the sediments on the cavern walls under three different geometric constraints: cylindrical, spherical, and conical caverns. The comparison results are shown in Fig. 20.

Regarding the vertical stress distribution, both the hydrostatic pressure and the vertical sediment stress in the cylindrical cavern increase monotonically with sediment accumulation depth. In contrast, the vertical sediment stresses in the spherical and conical caverns initially increase and then decrease, with peak stresses occurring in the middle-to-lower regions of the caverns. At the same depth, the hydrostatic pressure is the highest, followed by the vertical sediment pressures in the cylindrical and spherical caverns, while the conical cavern exhibits the lowest vertical pressure. Moreover, the differences in vertical stress among the different cavern geometries increase continuously with sediment accumulation depth. In the upper and middle regions of the sediments, the vertical pressures in the cylindrical and spherical caverns differ only slightly because the wall curvature of the spherical cavern changes relatively little in its upper region, resulting in a geometry similar to that of a cylindrical cavern. As the sediment accumulation depth increases, the cross-sectional area of the spherical cavern decreases, reducing the additional sediment weight per unit depth and consequently causing a decrease in vertical stress near the cavern bottom. Compared with the spherical cavern, the vertical sediment pressure in the conical cavern decreases more rapidly, reaching zero at the sediment bottom.

Regarding the normal pressure exerted by sediments on cavern walls, the three cavern geometries exhibit distinct pressure distributions. The hydrostatic pressure remains the highest, followed by the normal pressure in the spherical cavern. The normal pressure in the conical cavern is higher than that in the cylindrical cavern in the upper sediment

region but becomes lower near the cavern bottom. This is because the wall of the spherical cavern gradually transitions from vertical to horizontal, and the lateral pressure coefficient progressively increases with depth until the normal pressure exerted on the cavern wall equals the vertical pressure at the lowest point. Consequently, the normal pressure continues to increase with depth, exhibiting only a slight decrease near the cavern bottom. In contrast, the wall inclination angles of the cylindrical and conical caverns remain constant. However, the lateral pressure coefficient of the conical cavern is greater than that of the cylindrical cavern with vertical walls, resulting in higher normal pressure in the upper sediment region. Near the conical bottom, the cross-sectional area decreases sharply, leading to a rapid reduction in pressure.

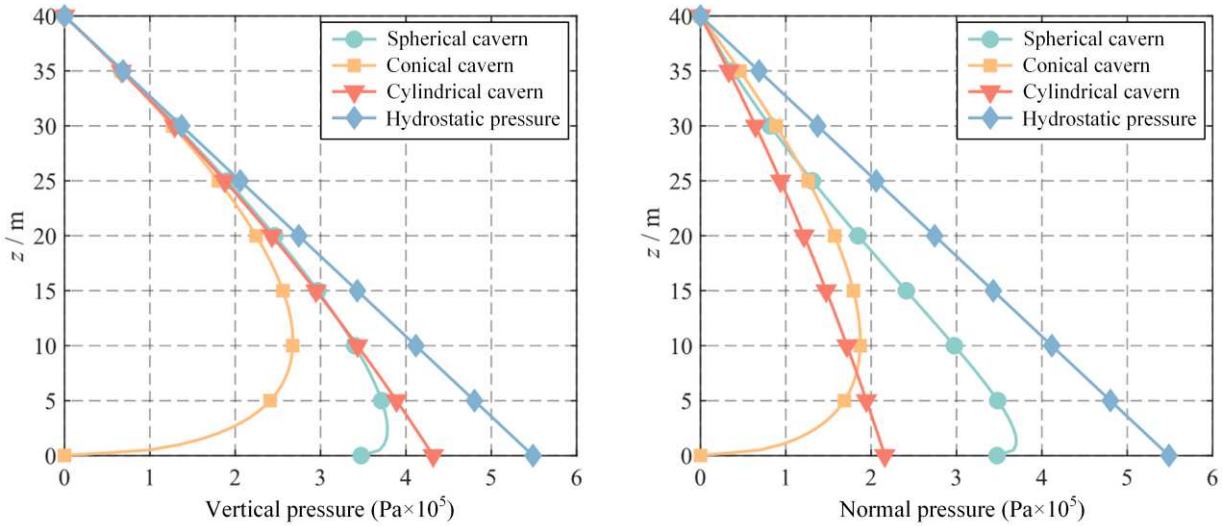


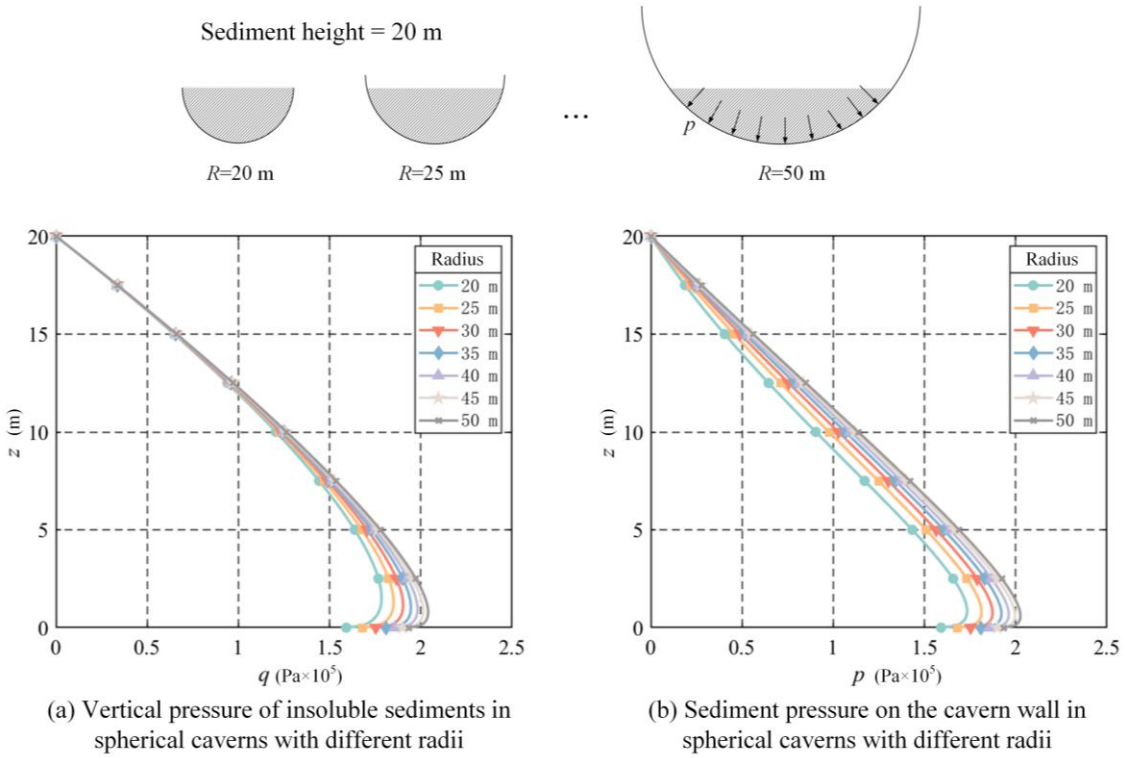
Fig. 20. Sediment pressure between different cavern shapes

Based on the above analysis, the commonly used hydrostatic pressure-based estimation method overestimates the normal pressure exerted by sediments on cavern walls and, consequently, their supporting effect, potentially leading to inaccurate assessments of salt cavern stability.

4.2.2 Spherical cavern radius

To investigate the influence of the spherical cavern radius on sediment pressure, the radius of the spherical cavern was set to range from 20 m to 50 m, while the sediment accumulation height was fixed at 20 m. The remaining parameters were kept the same as those in the engineering case study. The distributions of vertical sediment pressure and normal pressure under different cavern radii were then calculated, and the results are shown in Fig. 21.

With regard to the distribution characteristics of vertical sediment pressure, at the same accumulation depth, a larger spherical cavern radius corresponds to a higher vertical sediment pressure, and the location of the peak stress is closer to the cavern bottom. However, the differences in vertical sediment pressure among spherical caverns with different radii are generally small. Taking the stress at the cavern bottom as an example, when the cavern radius is 20 m, the vertical sediment pressure at the bottom is 0.177 MPa; when the cavern radius increases to 50 m, the bottom stress increases to 0.204 MPa, representing an increase of only 15%. This is because, when the boundary conditions at the cavern wall do not vary significantly, sediment pressure is governed primarily by the accumulation depth. In the upper sediment region, stress is transmitted mainly in the vertical direction and increases approximately linearly. Near the cavern bottom, the curvature constraint of the spherical cavern becomes stronger, and part of the vertical stress is transferred to the cavern wall through interparticle contacts, thereby slowing the increase in vertical pressure. As the spherical cavern radius increases, the wall curvature decreases and the arching effect becomes weaker; consequently, the vertical pressure becomes higher and its linear characteristic becomes more pronounced.



(a) Vertical pressure of insoluble sediments in spherical caverns with different radii

(b) Sediment pressure on the cavern wall in spherical caverns with different radii

Fig. 21. Sediment pressure distribution in spherical caverns with different wall radii

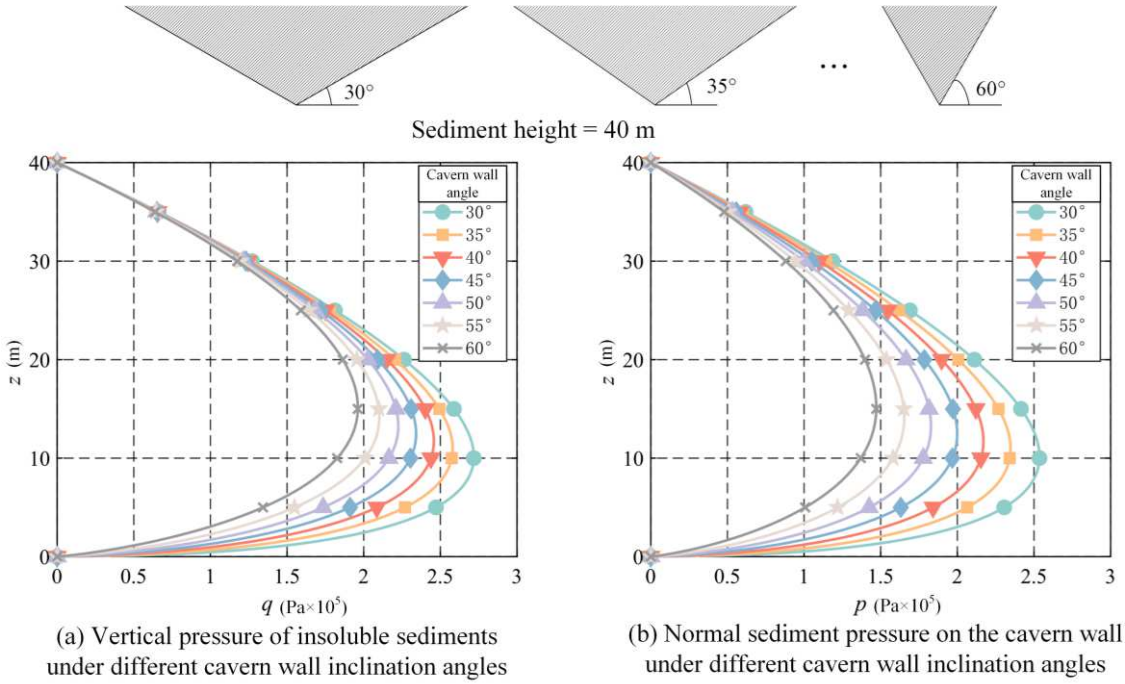
Regarding the normal pressure exerted by the sediments on the cavern wall, the differences among caverns with different spherical radii are slightly greater than those in vertical pressure, but they still remain within a relatively small range overall. This is because the normal pressure acting on the cavern wall is transferred from the vertical pressure through the lateral pressure coefficient. For spherical caverns with different radii, the variation in the lateral pressure coefficient with depth is relatively small within the limited region near the bottom. Therefore, the distribution pattern of normal pressure in spherical caverns is similar to that of vertical sediment pressure.

4.2.3 Conical cavern wall inclination angle

To investigate the influence of the conical cavern wall inclination angle on sediment pressure, the wall inclination angle α_w was varied from 30° to 60°, while the sediment accumulation height was fixed at 40 m. The remaining parameters were kept identical to those in the engineering case study, and the lateral pressure coefficient was determined using Eq. (21). The sediment pressure distributions under different wall inclination angles were calculated, and the results are shown in Fig. 22.

The results indicate that the normal pressure in the conical cavern initially increases and then decreases with depth, reaching a peak value of 0.15–0.25 MPa at approximately 10–15 m above the cavern bottom before decreasing to zero at the conical bottom. This indicates that the sediments exert the strongest supporting effect on the middle-to-lower region of the conical cavern, whereas their supporting effect is relatively weak at the cavern bottom and in the upper sediment region. Therefore, particular attention should be paid to the stability of the cavern bottom in engineering design. Comparing the cases with different wall inclination angles, the peak sediment pressure in the 30° cavern occurs 5 m higher than that in the 60° cavern. Although the cavern volume increases by 200%, the peak sediment pressure increases by only 70%.

This indicates that, compared with caverns in high-grade salt deposits, caverns with higher insoluble contents may contain larger volumes of sediments, but this does not necessarily result in higher supporting pressure. The effects of cavern geometry and sediment accumulation depth are equally important.



(a) Vertical pressure of insoluble sediments under different cavern wall inclination angles

(b) Normal sediment pressure on the cavern wall under different cavern wall inclination angles

Fig. 22. Sediment pressure in conical caverns with different wall angles

4.2.4 Sediment accumulation height

This section focuses on the cylindrical–spherical and cylindrical–conical combined caverns, which are the most common geometries encountered in engineering practice. The cavern geometric parameters and sediment properties were kept constant, while the sediment accumulation height was varied from 10 to 70 m to investigate its influence on the pressure distribution. The results are shown in Fig. 23. It can be observed that, in the cylindrical–conical cavern, the normal pressure exerted by the sediments on the cavern wall exhibits an abrupt change at the interface between the cylindrical and conical sections. This is because the cavern wall inclination angle and lateral pressure coefficient change across the interface, resulting in a sharp increase in the normal sediment pressure at the interface on the conical side.

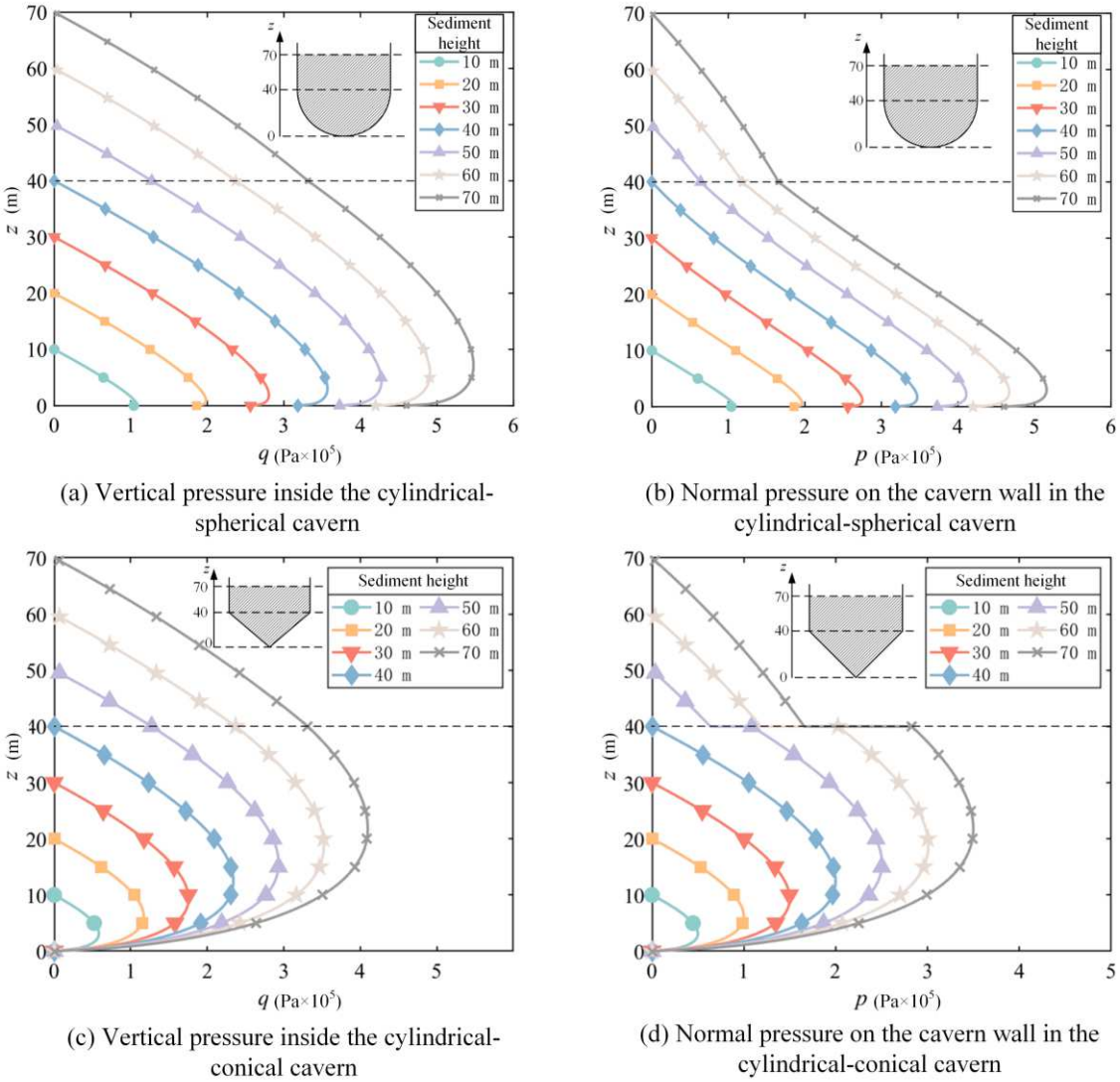
Furthermore, in the spherical and cylindrical–spherical caverns, both the vertical and normal sediment pressures reach their maximum values near the cavern bottom before decreasing. In contrast, the sediment pressures in the conical and cylindrical–conical caverns not only decrease near the bottom but also diminish to zero at the lowest point of the cavern. This is because the cross-sectional area decreases toward the cavern bottom, where the incremental gravitational force of the sediments per unit height becomes smaller than the supporting force component provided by the cavern walls, resulting in a reduction in pressure.

For salt cavern gas storage facilities at burial depths exceeding 1000 m, the operating pressure typically exceeds 10 MPa. The supporting pressure provided by accumulated sediments is relatively small compared with the internal gas pressure, and thus the improvement in salt cavern stability due to sediments is generally limited. However, the supporting effect of sediments cannot be neglected under the following conditions:

(1) Shallow salt caverns. When salt caverns are located at relatively shallow depths, both the in situ stress and operating pressure are considerably lower than those in deep salt caverns. Consequently, the contribution of sediment pressure to cavern stability becomes more pronounced.

(2) Salt caverns with sediment accumulation heights exceeding 100 m. As solution mining continues, the total cavern height can exceed 200 m, and the sediment accumulation height within the cavern can also exceed 100 m.

(3) Gas storage caverns operating at minimum pressure. During gas storage operations, when the internal pressure reaches its minimum value during the gas withdrawal phase, the supporting pressure acting on the cavern walls is at its lowest level. Under these conditions, the contribution of sediments to cavern stability becomes particularly significant.



(a) Vertical pressure inside the cylindrical-spherical cavern

(b) Normal pressure on the cavern wall in the cylindrical-spherical cavern

(c) Vertical pressure inside the cylindrical-conical cavern

(d) Normal pressure on the cavern wall in the cylindrical-conical cavern

Fig. 23. Sediment pressure distribution in caverns with different sediment accumulation heights

4.2.5 Cavern wall friction coefficient

Taking the spherical cavern as an example, the influence of the friction coefficient μ between the sediments and the cavern wall on the sediment pressure distribution was investigated. The distributions of normal pressure under different friction coefficients are shown in Fig. 24.

The results indicate that the friction coefficient has a relatively minor influence on sediment pressure in the upper half of the spherical cavern but a pronounced influence in the lower half. Moreover, a lower friction coefficient results in greater normal pressure exerted by the sediments on the cavern wall. This is because a lower friction coefficient weakens the frictional restraint exerted by the cavern wall on the sediments, causing a greater proportion of the sediment self-weight-induced stress to be transferred to the cavern wall through normal pressure.

From the perspective of the force transmission mechanism, the cavern wall in the middle-to-lower region of the spherical cavern has a smaller inclination angle and primarily bears the vertical pressure component of the sediments,

whereas the wall in the middle-to-upper region has a larger inclination angle and mainly bears lateral pressure. Consequently, variations in the friction coefficient have a more pronounced influence on the pressure in the middle-to-lower region. Furthermore, when the friction coefficient is relatively high, the cavern wall provides greater upward frictional support. Within a very small region near the cavern bottom, the increase in upward frictional support may exceed the increase in sediment self-weight loading, resulting in a decrease in both vertical and normal pressures.

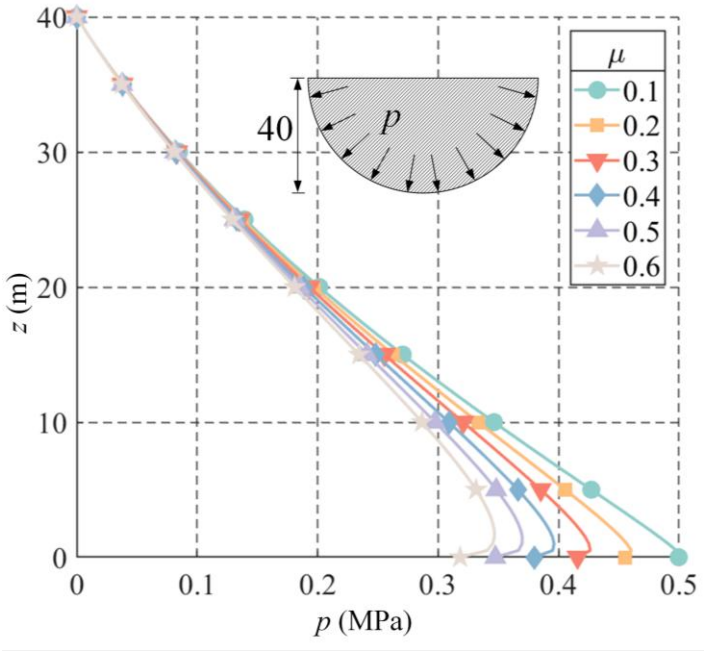


Fig. 24. Sediment pressure distribution in caverns with different friction parameters

5 Conclusion

This study derived equations for calculating sediment pressure in salt caverns with different geometries based on the Janssen equation. The proposed method was validated through comparative analyses between PFC^{3D}–FLAC^{3D} coupled simulations and FLAC^{3D} simulations incorporating the derived equations. An engineering case study and parametric analyses were also conducted. The main conclusions are as follows:

(1) A geometry-dependent sediment-pressure formulation based on the Janssen equation was developed for cylindrical, conical, spherical, cylindrical–conical, and cylindrical–spherical salt caverns. By accounting for the geometric characteristics of individual cavern sections, the formulation provides equations for both vertical sediment pressure and the normal pressure exerted by sediments on cavern walls.

(2) (2) Validation against the PFC^{3D}–FLAC^{3D} coupled benchmark model showed that the absolute difference in sediment pressure did not exceed 0.03 MPa. When the proposed formulation was implemented in FLAC^{3D}, the absolute error in the calculated displacement was less than 5 mm, and the relative error remained within ±5% compared with the coupled model. For the case examined, the computation time was reduced from approximately one month for the coupled simulation to four days for the FLAC^{3D} model, demonstrating a substantial improvement in computational efficiency while maintaining close agreement with the benchmark result.

(3) The supporting effect of sediments on salt cavern stability and its engineering significance were clarified. The engineering case study demonstrated that the normal pressure exerted by sediments can effectively supplement the supporting pressure acting on cavern walls. Under the minimum operating pressure condition, the total supporting pressure at the cavern bottom increased by 15.4%, and the ratio of total supporting pressure to in situ stress at the

cavern bottom increased from 30.1% to 34.6%, significantly improving the stress state of the cavern bottom, which represents a critical region for stability control. These findings have important engineering implications for ensuring the stability of salt cavern gas storage facilities in high-impurity salt deposits.

(4) Cavern geometry and sediment accumulation height significantly influence the distribution of sediment pressure, whereas the effect of cavern radius is relatively limited within the investigated range. In cylindrical caverns, the normal pressure increases monotonically with sediment depth, while in spherical and conical caverns, it generally reaches a peak before decreasing toward the cavern bottom. Furthermore, increasing the friction coefficient between the sediments and cavern wall reduces the normal pressure, particularly in the lower region of spherical caverns, where a localized pressure decrease may occur near the bottom under relatively high friction conditions.

Acknowledgments

This work was supported by the National Natural Science Foundation of China (Grant No. 42177124), Open Research Fund of State Key Laboratory of Geomechanics and Geotechnical Engineering, Institute of Rock and Soil Mechanics, Chinese Academy of Sciences (Grant No. SKLGME022011), Frontier Technologies R&D Program of Jiangsu (Grant No. BF2024056).

References

Bo Y, Wang H, Jiang M, et al (2022) Particle size effect of tunnel mechanical state in discrete element simulation. Chin J Undergr Space Eng 18(5):1471–1480.

Chen X, Zhu W (1996) Extension and application of Janssen equation. China Civ Eng J (5):11–17.

Cording E, Hashash Y, Oh J (2015) Analysis of pillar stability of mined gas storage caverns in shale formations. Eng Geol 184:71–80.

Cyran K (2021) The influence of impurities and fabrics on mechanical properties of rock salt for underground storage in salt caverns – a review. Arch Min Sci 66(2):155–179.

Deng J, Yang Q, Liu Y (2014) Time-dependent behaviour and stability evaluation of gas storage caverns in salt rock based on deformation reinforcement theory. Tunn Undergr Space Technol 42:277–292.

Djizanne H, Bérest P, Brouard B (2014) The mechanical stability of a salt cavern used for compressed air energy storage (CAES). In: Proceedings of the 2014 Spring SMRI Technical Conference, San Antonio, Texas, USA.

Fan J, Tang L, Fourmeau M, Li Z, Liu W, Zou Y, et al (2025) A novel viscoplastic model for salt rock deformation under internal cyclic gas pressure loading. Int J Min Sci Technol 35(6):989–1004.

Fatah A, Al-Yaseri A, Theravalappil R, et al (2024) Geochemical reactions and pore structure analysis of anhydrite/gypsum/halite bearing reservoirs relevant to subsurface hydrogen storage in salt caverns. Fuel 371:131857.

Fu L, Shi X, Fan J, et al (2025) Safety evaluation system of salt cavern hydrogen storage based on matter-element extension method. J Energy Storage 116:116028.

Gao S, Ban F, Shan W, et al (2005) The influence of rock salt insoluble matter content on volume's effective rate of utilization of gas storage in salt caverns building with water solution. Rock Soil Mech 26(S2):179–183.

Ge X, Li Y, Li J, et al (2023) Falling behavior and application of interlayer-collapse-formed blocks during solution mining in salt cavern storages. Chin J Rock Mech Eng 42:918–929.

Gu X, Lu L, Qian J (2017) Discrete element modeling of the effect of particle size distribution on the small strain stiffness of granular soils. Particuology 32:21–29.

He Q, Liu J, Wu F, Li C, Chen J, Gao R, et al (2025) Fatigue properties and constitutive model of Jintan salt rock subjected to complex cyclic loading. Int J Min Sci Technol 35(1):121–133.

Hu B, Yu L, Mi X, Xu F, Li S, Li W, et al (2024) Comparative analysis of thermodynamic and mechanical responses between underground hydrogen storage and compressed air energy storage in lined rock caverns. Int J Min Sci Technol 34(4):531–543.

Hua Y, Feng Y (1994) Plastic limit analysis of circular silos. Eng Mech (3).

Janssen HA (1895) Versuche über Getreidedruck in Silozellen. Z Ver Deut Ing 39:1045.

Khaledi K, Mahmoudi E, Datcheva M, et al (2016) Stability and serviceability of underground energy storage caverns in rock salt subjected to mechanical cyclic loading. Int J Rock Mech Min Sci 86:115–131.

Kumar KR, Makhmutov A, Spiers CJ, et al (2021) Geomechanical simulation of energy storage in salt formations. Sci Rep 11(1):19640.

Lei Y, Ma Q, Shi Q (2019) Side-wall pressure distribution of cylindrical granular containers with flat bottom. Powder Technol 353:57–63.

Li J, Shi X, Wang T, et al (2016a) A prediction model of the accumulation shape of insoluble sediments during the leaching of salt cavern for gas storage. J Nat Gas Sci Eng 33:792–802.

Li P, Li Y, Shi X, et al (2022) Compaction and restraining effects of insoluble sediments in underground energy storage salt caverns. Energy 249:123752.

Li P, Li Y, Shi X, Yang K, Wei X, Zhao K, et al (2023) Theoretical and numerical simulation studies of the self-stabilization capability of salt cavern roofs. Comput Geotech 163:105719.

Li Y, Ma H, Shi X, et al (2024) The challenges and countermeasure researches of salt cavern underground storage in China: from “Jintan mode” to “XX Mode”. Rock Soil Mech 45(10):1–11.

Li Y, Shi X, Liu W, et al (2016b) Motion of insoluble subsidence during leaching sump for salt cavern storage. Chin J Rock Mech Eng 35(1):23–31.

Li Z, Liu J, Deng C, et al (2018) Experimental study on deformation and failure characteristics of salt rock three-point-bending samples with impurities. Chin J Geotech Eng 40(S2):101–106.

Liang X, Ma H, Cai R, et al (2023a) Feasibility analysis of natural gas storage in the voids of sediment within salt cavern—a case study in China. Energy 285:129340.

Liang X, Ma H, Cai R, et al (2023b) Study of impact of sediment on the stability of salt cavern underground gas storage. Energies 16:7825.

Liu H, Cheng X (2009) Discrete element analysis for size effects of coarse-grained soils. Rock Soil Mech 30(S1):287–292.

Liu Y (2011) Brief discussion on the cause and prevention of the pipe plugging caused by salt crystal and sand in docking connectivity ming. China Well Rock Salt 42:19–21.

Liu W, Zhang X, Li H, Chen J (2020) Investigation on the deformation and strength characteristics of rock salt under different confining pressures. Geotech Geol Eng 38:5703–5717.

Liu W, Li Q, Yang C, et al (2023) The role of underground salt caverns for large-scale energy storage: a review and prospects. Energy Storage Mater 63:103045.

Liu Y, Zhang G, Wang Z, Li H, Zhang H, Liu K (2024) Bipolar coordinate solution of pillar stability for salt cavern energy storage. Comput Geotech 173:106506.

Ma H, Yang C, Li Y, et al (2015) Stability evaluation of the underground gas storage in rock salts based on new partitions of the surrounding rock. Environ Earth Sci 73:6911–6925.

Ma L, Liu X, Fang Q, et al (2013) A new elasto-viscoplastic damage model combined with the generalized Hoek–Brown failure criterion for bedded rock salt and its application. Rock Mech Rock Eng 46:53–66.

Martin-Clave C, Ougier-Simonin A, Vandeginste V (2021) Impact of second phase content on rock salt rheological behavior under cyclic mechanical conditions. Rock Mech Rock Eng 54:5245–5267.

Qu D, Shi X, Li Y, et al (2012) Engineering practice and analysis of limit roof diameter in building sump of salt cavern for gas storage. Chin J Rock Mech Eng 31(S2):3703–3709.

Ren Z, Li J, Ba J, et al (2017) Expansion technology for deposits of bottom in salt-rock gas storage and its application. Nat Gas Technol Econ 11(5):43–45+83.

Saleh K, Golshan S, Zarghami R (2018) A review on gravity flow of free-flowing granular solids in silos – basics and practical aspects. Chem Eng Sci 192:1011–1035.

Shi X, Li Y, Yang C, et al (2011) Collapse control technology for interbeds in solution mining for oil/gas storage in multi-interbedded salt formation. Chin J Geotech Eng 33(12):1957–1963.

Sperl M (2005) Experiments on corn pressure in silo cells – translation and comment of Janssen's paper from 1895. Granul Matter 8:59–65.

Sun C, Hou J, Ding G, et al (2017) Study on sedimentation rule of insoluble residual particles in brine of salt cavern underground gas storage. J Salt Sci Chem Ind 46:10–12.

Sun X, Ding G, Li K, et al (2024) Research on the influencing factors of the void volume of insoluble sediment in salt cavern gas storage. Processes 12:636.

Tang J, Lu H, Guo X, et al (2021) Static wall pressure distribution characteristics in horizontal silos. Powder Technol 393:342–348.

Vitali OPM, Vitali FPM (2024) Influence of overburden rock characteristics on stress arching and surface subsidence over salt caverns. Geotech Geol Eng 42:4245–4255. https://doi.org/10.1007/s10706-024-02773-w.

688 Walters J (1973) A theoretical analysis of stresses in silos with vertical walls. Chem Eng Sci 28:13–21.
689 Wang J, Liu X, Zhang Q, Liu X, Song Z, Feng S (2024a) Fatigue properties and damage constitutive model of salt
690 rock based on CT scanning. Int J Min Sci Technol 34(2):245–259.
691 Wang Q (2003) Solution mining of salt deposits. Chemical Industry Press.
692 Wang S, Wang H, Zhu H, Wu Z, Li Z (2023) Long-term stability analysis of pillars in salt cavern storage based on
693 the salt rock dilatancy boundary evaluation method. Geotech Geol Eng 41:3349–3358.
694 https://doi.org/10.1007/s10706-023-02459-9.
695 Wang T, Chai G, Cen X, et al (2021) Safe distance between debrining tubing inlet and sediment in a gas storage
696 salt cavern. J Pet Sci Eng 196:107707.
697 Wang T, Yan X, Yang H, et al (2013) A new shape design method of salt cavern used as underground gas storage.
698 Appl Energy 104:50–61.
699 Wang T, Yang C, Yan X, et al (2015) Allowable pillar width for bedded rock salt caverns gas storage. J Pet Sci
700 Eng 127:433–444.
701 Wang Z, Yuan G, Ban F, et al (2020) Experimental study on using residue void space in butt well salt cavern gas
702 storage. China Well Rock Salt 51(5):27–30.
703 Wanyan Q, Ran L, Han B, et al (2015) Study on site selection and evaluation of underground gas storage in salt
704 cavern. J Southwest Pet Univ (Sci Technol Ed) 37:57–64.
705 Wei X, Shi X, Li Y, et al (2023) Advances in research on gas storage in sediment void of salt cavern in China.
706 Energy 284:129243.
707 Wei X, Shi X, Ma H, et al (2024) Experimental investigation on the oil extraction process for a novel underground
708 oil storage method: oil storage in salt cavern insoluble sediment voids. Energy 309:133061.
709 Yan Z, Wang Z, Wu F, et al (2022) Stability analysis of Pingdingshan pear-shaped multi-mudstone interbedded salt
710 cavern gas storage. J Energy Storage 56:105963.
711 Ye L, Li H, Shi J, Chen F, Zou W (2025) Surface subsidence risk assessment for gas storage in salt caverns: effects
712 of depth and strata properties. Geotech Geol Eng 43:429. https://doi.org/10.1007/s10706-025-03402-w.
713 Yuan F, Pang K, Dong C, et al (2016) The PFC3D numerical simulation on dynamic pressures and flow of
714 sidedraw silos. Eng Mech 33(S1):301–305.
715 Zeng Z, Ma H, Liang W, Wang X, Liu F, Li W, et al (2025) Phase field modeling of crack self-healing kinetics in
716 wet rock salt: Theory, numerical implementation, and micro-CT validation. Comput Geotech 188:107598.
717 Zhang G, Li Y, Daemen JJK, et al (2015) Geotechnical feasibility analysis of compressed air energy storage
718 (CAES) in bedded salt formations: a case study in Huai'an city, China. Rock Mech Rock Eng 48(5):2111–2127.
719 Zhang G, Liu Y, Wang T, et al (2021a) Pillar stability of salt caverns used for gas storage considering sedimentary
720 rhythm of the interlayers. J Energy Storage 43:103229.

721 Zhang G, Wang L, Wu Y, et al (2017a) Failure mechanism of bedded salt formations surrounding salt caverns for
722 underground gas storage. Bull Eng Geol Environ 76(4):1609–1625.
723 Zhang G, Wang Z, Liu Y, et al (2021b) Research on stability of the key roof above horizontal salt cavern for
724 compressed air energy storage. Rock Soil Mech 42(3):800–812.
725 Zhang H, Yu H, Wang L, et al (2017b) Granularity distribution characteristics of deposits at the bottom of salt rock
726 gas storage based on fractal theory. Transportation & Storage 36(3):279–283.
727 Zhang H, Yu H, Wang L, et al (2024) Thermo-mechanical coupling analysis of deformation and failure of salt
728 cavern UGS under the influence of sediment particles. Nat Gas Ind 44(12):137–150.
729 Zhang N, Shi X, Wang T, et al (2017c) Stability and availability evaluation of underground strategic petroleum
730 reserve (SPR) caverns in bedded rock salt of Jintan, China. Energy 134:504-514.